




RESEARCH ARTICLE | MARCH 19 2024

## On the airfoil leading-edge noise reduction using poro-wavy leading edges

Weijie Chen (陈伟杰) ; Hui Lei (雷辉); Yudi Xing (邢玉迪); Liangfeng Wang (王良锋); Teng Zhou (周腾)  ; Weiyang Qiao (乔渭阳)



*Physics of Fluids* 36, 035158 (2024)

<https://doi.org/10.1063/5.0198034>



## APL Energy

### Latest Articles Online!

[Read Now](#)



# On the airfoil leading-edge noise reduction using poro-wavy leading edges

Cite as: Phys. Fluids **36**, 035158 (2024); doi: [10.1063/5.0198034](https://doi.org/10.1063/5.0198034)

Submitted: 16 January 2024 · Accepted: 6 March 2024 ·

Published Online: 19 March 2024





View Online



Export Citation



CrossMark

Weijie Chen (陈伟杰),<sup>1,2</sup>  Hui Lei (雷辉),<sup>1</sup> Yudi Xing (邢玉迪),<sup>1</sup> Liangfeng Wang (王良锋),<sup>3</sup> Teng Zhou (周腾),<sup>4,a)</sup>  and Weiyang Qiao (乔渭阳)<sup>1,2</sup>

## AFFILIATIONS

<sup>1</sup>School of Power and Energy, Northwestern Polytechnical University, Xi'an, Shaanxi 710129, China

<sup>2</sup>Laboratory of Aerodynamic Noise Control, China Aerodynamics Research and Development Center, Mianyang, Sichuan 621000, China

<sup>3</sup>High Speed Aerodynamic Institute, China Aerodynamics Research and Development Center, Mianyang, Sichuan 621000, China

<sup>4</sup>School of Engineering, University of Southampton, SO17 1BJ, United Kingdom

<sup>a)</sup> Author to whom correspondence should be addressed: [T.zhou@soton.ac.uk](mailto:T.zhou@soton.ac.uk)

## ABSTRACT

This paper presents numerical studies on airfoil leading-edge turbulence interaction noise reduction using poro-wavy leading edges. Three different bionic treatments including wavy leading edges, porous leading edges, and a novel combined poro-wavy leading edges are modeled. The turbulent flow field is solved using the improved delayed detached eddy simulation method. The aerodynamic noise is predicted using the Ffowcs Williams and Hawkins acoustic analogy theory. The inflow Mach number is approximately 0.12 with an angle of attack of 0°, and the chord-based Reynolds number is 400 000. The present numerical method is first validated against experimental data and previous studies. Then the effects of the three bionic treatments on the aerodynamic performance and the aeroacoustic performance are analyzed. The results show that all the three bionic treatments will increase the mean drag of the airfoil, especially for the airfoils with porous treatment, while the lift and drag fluctuations are significantly reduced by the three bionic treatments. The wavy leading edges are found to be more effective for the reduction of broadband noise, while the porous leading edges are more effective for the reduction of the tonal noise. For the poro-wavy leading edges, both the tonal noise and broadband noise are significantly reduced, which means that the combined poro-wavy leading edges possess both the advantages of the wavy and porous treatments. The underlying flow mechanisms responsible for the noise reduction are finally analyzed in detail.

© 2024 Author(s). All article content, except where otherwise noted, is licensed under a Creative Commons Attribution (CC BY) license (<https://creativecommons.org/licenses/by/4.0/>). <https://doi.org/10.1063/5.0198034>

## I. INTRODUCTION

The interaction of incoming turbulence with the leading edge of an airfoil will radiate intensive noise.<sup>1</sup> The leading-edge noise generated by the interaction of the rotor wake with the outlet guide vanes (OGV) is the dominant sound source in modern high-bypass ratio turbofan engines.<sup>2</sup> The control of fan noise is the key for the future green aviation concept.<sup>3</sup> In order to overcome the fan wake-OGV interaction noise, bionic treatments inspired by nature have been proposed as passive noise reduction technologies over the past few years. The wavy leading edges bioinspired by humpback whale flippers have been found to be very effective for noise reduction. The reduction of airfoil turbulence interaction noise using wavy leading edges has been the subject of many experimental,<sup>4–10</sup> numerical,<sup>11–16</sup> and theoretical studies.<sup>17–22</sup>

Chaitanya *et al.* performed parametric experimental studies on the effectiveness of sinusoidal leading-edge serrations on airfoil

turbulence interaction noise.<sup>4</sup> One of the most important findings of this paper is that, an optimum serration wavelength is identified, which is approximately four times the transverse integral length scale of the incoming turbulence. Different from using single-wavelength serrations, Chaitanya *et al.* further proposed double-wavelength serrations to improve the noise reduction level of the leading-edge serrations.<sup>5</sup> Significantly greater noise reductions are achieved by the new noise control concept, through destructive interference between different parts of the airfoil leading edge. Drawing inspiration from Chaitanya's idea, Narayanan *et al.* conducted an experimental study on airfoil turbulence interaction noise reduction through multi-wavelength leading-edge serrations.<sup>6</sup> They found that the double-wavelength serrations act as the best modifications for achieving the highest noise reductions as compared to the single- and triple-wavelength serrations. A family of serration profiles including double-wavelength, chopped-peak,

slitted-root, variable-slit, and slitted serration was further proposed by Chaitanya *et al.* to enhance the noise reduction level.<sup>7</sup> The results show that, this new family of profiles provides considerably greater noise reductions than single-wavelength serrations, and a fundamentally different noise reduction mechanism is found for the new type of profiles. A novel ogee serration was proposed and compared to conventional sawtooth serrations by Lyu *et al.*<sup>8</sup> It is found that ogee serrations are superior to conventional serrations within the whole frequency range of interest. The above-mentioned experimental studies all use isotropic turbulence generated by the upstream turbulence grids to interact with the downstream airfoil. A tandem rod-airfoil flow configuration and a tandem airfoil-airfoil flow configuration were used by the present authors<sup>9</sup> and Vemuri *et al.*,<sup>10</sup> respectively, to examine the noise reduction effect under anisotropic inflow turbulence. It was observed that a notable noise reduction level can also be achieved under wake inflow conditions.

Full three-dimensional Euler equation was solved by Kim *et al.* to reveal noise reduction mechanisms of sinusoidal serrations.<sup>11</sup> Two main noise reduction mechanisms named source-cutoff effect and phase interference effect are identified. Full three-dimensional Euler solutions were further computed by Turner and Kim to explain the universal trends in the noise reduction due to wavy leading edges.<sup>12</sup> The results show that the high-frequency noise reduction is driven almost entirely by destructive phase interference. Large eddy simulations and Ffowcs Williams and Hawkins (FW-H) acoustic analogy theory were used by the present authors on a rod-airfoil configuration to study the noise reduction effect of wavy leading edges.<sup>13</sup> One of the most important findings is that there exists intensive noise source around the trough region of the wavy leading edges. Based on a rectilinear seven-vane cascade rig, Nuszyk *et al.* performed a numerical study on turbulence-cascade noise reduction from serrations.<sup>14</sup> A modified Fourier modes-based method was used to generate the incoming turbulence, while the unsteady fluctuations on the vane surface were computed using the linearized Euler equation, and the far-field noise was evaluated by the FW-H equation. An overall sound reduction level around 4–6 dB is obtained. In addition to the work on two-dimensional airfoils and cascades, numerical studies have also been performed on aero-engine fans. Using a hybrid unsteady Reynolds averaged Navier–Stokes (URANS) and acoustic analogy method, the present authors conducted a numerical study on the noise reduction effect of wavy leading edges on a low-speed single-stage axial-flow fan.<sup>15</sup> It is found that the serration with larger amplitude achieves better noise reduction with a maximum tonal noise reduction level of 4.3 dB. It is also notable that intensive noise source is observed at each trough region of the wavy stator. Based on a hybrid lattice-Boltzmann/very-large-eddy-simulation model, Casalino *et al.* performed studies of a wavy stator leading edge in a realistic fan/OGV stage.<sup>16</sup> It is found that noise reduction can be achieved when the serration amplitude and wavelength are large enough compared to the integral scales of the impinging turbulence.

A theoretical model was proposed by Huang to study the scattering of sound waves from a serrated flat plate by incorporating Fourier series expansions and the Wiener–Hopf method.<sup>17</sup> The model is validated against a commercial finite element solver and can evaluate the noise reduction level of serrations with high-efficiency. An analytical model was developed by Lyu and Azarpeyvand to predict the noise radiated by an airfoil with leading-edge serrations by using Fourier

expansion and Schwarzschild techniques.<sup>18</sup> The model demonstrates that the destructive interference of the scattered pressure induced by the leading-edge serrations is the main noise reduction mechanism. An analytical model was proposed by Ayton and Kim for the prediction of the noise generated by an unsteady gust interacting with a semi-infinite flat plate with serrated leading edges by using the Wiener–Hopf method and separation of variables.<sup>19</sup> They found a logarithmic dependence between the tip-to-root serration height and the decrease in far-field noise. The underlying noise reduction mechanisms are attributed to the destructive interference and a redistribution of acoustic energy from low cut-on modes to higher cutoff modes. Using similar methods, Ayton and Chaitanya further improved the analytical model that can be used to predict the gust-airfoil interaction noise for flat plates with spanwise-varying periodic leading edges.<sup>20</sup> Based on the theoretical model, Lyu *et al.* provided guides for the optimal serration geometry.<sup>21</sup> They pointed out that piecewise smooth profiles free of stationary points are more effective for noise reduction, and a remarkable 7 dB additional noise reduction is obtained by using the new serration design. By approximating an infinite-interval integral involving two infinite sums to a single straightforward sum, Lyu and Ayton developed rapid noise prediction models for serrated leading and trailing edges, which are of particular importance for numerical optimization applications.<sup>22</sup>

Except for the wavy leading edges, porous treatments have also been used for the reduction of airfoil turbulence interaction noise. Based on a rod-airfoil configuration, Zampni *et al.* conducted experimental studies on leading-edge noise reduction by means of porosity.<sup>23</sup> The results indicate that the porosity has noise reduction effects mainly on the low-frequency range. The upwash component of the root mean square (rms) of the velocity fluctuations is significantly reduced in the porous case in contrast to the solid one, which is thought to be the main noise reduction mechanism. Chaitanya *et al.* performed an experimental study on the reduction of turbulence-airfoil interaction noise by the introduction of airfoil porosity.<sup>24</sup> One of the main findings is that the noise reduction spectra collapse when plotted against non-dimensional frequency based on the length of porous section and the inflow velocity. The source cutoff effect and edge-to-edge destructive interference are proposed to be the two main noise reduction mechanisms. Cabre *et al.* performed experimental studies on the use of porosity located downstream of an airfoil leading edge for the reduction of turbulence interaction noise.<sup>25</sup> An overall noise reduction of up to 2.8 dB is achieved, and one of the main noise reduction mechanisms is a phase shift of 180° induced by the secondary vorticity generated at the leading edge. The effect of leading-edge porosity on airfoil turbulence interaction noise was also experimentally studied by Bowen *et al.*<sup>26</sup> The results demonstrate that the porosity can reduce the turbulence interaction noise in the low- to mid-frequency range, with a penalty of a high-frequency noise increase. Large eddy simulations and Curle's acoustic analogy model were solved by Zamponi *et al.* to investigate the effect of porosity on airfoil turbulence interaction noise.<sup>27</sup> The results demonstrate that the porous treatment can reduce the unsteady pressure peak, but it is ineffective in breaking the spanwise coherence of the surface pressure fluctuations.

From the aforementioned literature, it is clear that both the wavy leading edges and porous materials are effective passive noise control methods. The works of Vathylakis *et al.*<sup>28</sup> and Chong *et al.*,<sup>29</sup> who combine the trailing-edge serrations and porous materials to enhance

the trailing-edge noise reduction level, motivated this study. The purpose of the present study is to combine the wavy leading edges and porous materials to improve the leading-edge noise reduction level and reveal the noise reduction mechanisms of the different bionic treatments. The paper is organized as follows. Section II describes the numerical methods used for computing the flow field and far-field noise. The results and discussion are presented in Sec. III, including the effects of different bionic treatments on aerodynamic performance, aeroacoustic performance, and the noise reduction mechanisms. Finally, some conclusions are provided in Sec. IV.

## II. NUMERICAL METHODOLOGY

### A. Flow-field simulations

In this study, the shear stress transport (SST)-based improved delayed detached eddy simulation (IDDES) is performed to compute the turbulent flow field. The governing equations of the SST-based IDDES model are as follows:<sup>30</sup>

$$\begin{aligned} \frac{\partial \rho k}{\partial t} + \nabla \cdot (\rho \mathbf{U} k) &= \nabla \cdot [(\mu + \sigma_k \mu_t) \nabla k] + P_k - \rho \sqrt{k^3} / l_{IDDES}, \quad (1) \\ \frac{\partial \rho \omega}{\partial t} + \nabla \cdot (\rho \mathbf{U} \omega) &= \nabla \cdot [(\mu + \sigma_\omega \mu_t) \nabla \omega] \\ &+ 2(1 - F_1) \rho \sigma_{\omega 2} \frac{\nabla k \cdot \nabla \omega}{\omega} + \alpha \frac{\rho}{\mu_t} P_k - \beta \rho \omega^2, \quad (2) \end{aligned}$$

where  $\rho$  is the density,  $k$  is the turbulence kinetic energy,  $\mathbf{U}$  is the velocity,  $\mu$  is the molecular viscosity,  $\mu_t$  is the turbulent viscosity,  $P_k$  is the production term,  $\omega$  is the specific dissipation rate, and  $F_1$  is the SST blending function.  $\sigma_k$ ,  $\sigma_\omega$ ,  $\sigma_{\omega 2}$ ,  $\alpha$ , and  $\beta$  are the model constants. The IDDES length scale is computed as follows:

$$l_{IDDES} = \tilde{f}_d \cdot (1 + f_e) \cdot l_{RANS} + (1 - \tilde{f}_d) \cdot l_{LES}, \quad (3)$$

where  $\tilde{f}_d$  and  $f_e$  are the empiric blending function and elevating function, respectively. The RANS length scale and LES length scale are defined by

$$l_{RANS} = \frac{\sqrt{k}}{C_\mu \omega}, \quad (4)$$

$$l_{LES} = C_{DES} \Delta, \quad (5)$$

where  $C_\mu$  and  $C_{DES}$  are the model constants, and  $\Delta$  is the length scale of the grid cell.

### B. The porous media model

The Brinkman–Forchheimer extended Darcy model<sup>31,32</sup> is used to compute the flow in the isotropic and homogeneous porous medium. The governing equations are as follows:

$$\nabla \cdot \mathbf{u}_D = 0, \quad (6)$$

$$\begin{aligned} \rho \left[ \frac{\partial \mathbf{u}_D}{\partial t} + \nabla \cdot \left( \frac{\mathbf{u}_D \mathbf{u}_D}{\phi} \right) \right] &= -\nabla P + \mu \nabla^2 \mathbf{u}_D \\ &- \left[ \frac{\mu \phi \mathbf{u}_D}{K} + \frac{C_F \rho \phi \mathbf{u}_D |\mathbf{u}_D|}{\sqrt{K}} \right], \quad (7) \end{aligned}$$

where  $\mathbf{u}_D = \phi \langle \mathbf{u} \rangle$  is the Darcy velocity,  $\langle \mathbf{u} \rangle$  is the intrinsic averaged local velocity, and  $\phi$  is the porosity.  $\rho$  and  $\mu$  are the density and dynamic viscosity, respectively.  $P = \phi \langle p \rangle$ , where  $\langle p \rangle$  is the intrinsic averaged pressure of the fluid. The permeability  $K$  and inertial coefficient  $C_F$  of the porous medium are given as follows:<sup>33</sup>

$$K = \frac{d_p^2 \phi^3}{150(1 - \phi)^2}, \quad (8)$$

$$C_F = \frac{1.75}{\sqrt{150} \phi^{3/2}}, \quad (9)$$

where the permeability and inertial coefficient are computed by the mean diameter  $d_p$  of the particle and the porosity following Ergun's model.<sup>34</sup> The present porous media model is similar to that of Bae and Moon<sup>35</sup> who used a porous material for the trailing-edge noise reduction of a flat plate.

### C. Aerodynamic noise predictions

The far-field aerodynamic noise is predicted using the FW–H acoustic analogy theory,<sup>36</sup> with the fluctuating pressure obtained by IDDES as feeding data. By manipulating the continuity and momentum equations, the FW–H equation can be written as

$$\begin{aligned} \frac{1}{c_0^2} \frac{\partial^2 p'}{\partial t^2} - \nabla^2 p' &= \frac{\partial^2}{\partial x_i \partial x_j} [T_{ij} H(f)] - \frac{\partial}{\partial x_i} \{ [P_{ij} n_j + \rho u_i (u_n - v_n)] \delta(f) \} \\ &+ \frac{\partial}{\partial t} \{ [\rho_0 v_n + \rho (u_n - v_n)] \delta(f) \}, \quad (10) \end{aligned}$$

where  $c_0$  is the free-field sound speed,  $p' = p - p_0$  is the far-field acoustic pressure,  $f = 0$  is the source surface,  $u_i$  is the fluid velocity component in the  $x_i$  direction,  $u_n$  is the fluid velocity component normal to the source surface,  $v_i$  is the surface velocity component in the  $x_i$  direction,  $v_n$  is the surface velocity component normal to the surface,  $n_i$  is the unit normal vector pointing toward the exterior region,  $\delta(f)$  is the Dirac delta function,  $H(f)$  is the Heaviside function, and  $T_{ij}$  is the Lighthill's stress tensor defined by

$$T_{ij} = \rho u_i u_j + P_{ij} - c_0^2 (\rho - \rho_0) \delta_{ij}. \quad (11)$$

For a Stokes fluid, the compressive stress tensor  $P_{ij}$  is given by

$$P_{ij} = p \delta_{ij} - \mu \left( \frac{\partial u_i}{\partial x_j} + \frac{\partial u_j}{\partial x_i} - \frac{2}{3} \frac{\partial u_k}{\partial x_k} \delta_{ij} \right). \quad (12)$$

The integral solution of the FW–H equation was derived by Farassat in the time domain referred to as Formulation 1A,<sup>37</sup> which is used in the present study.

### D. Description of the different bionic treatments

In this paper, the NACA0012 (National Advisory Committee for Aeronautics, NACA) airfoil with a straight leading edge is used as the baseline airfoil. Three different bionic modifications named wavy leading edges, porous leading edges, and poro-wavy leading edges that combine the wavy and porous treatments are designed, as shown in Fig. 1. The wavy leading edges are characterized by the amplitude  $A$  (peak-to-trough length) and wavelength  $W$  (peak-to-peak length). The wavy airfoil used in this study is A20W10, which means that the

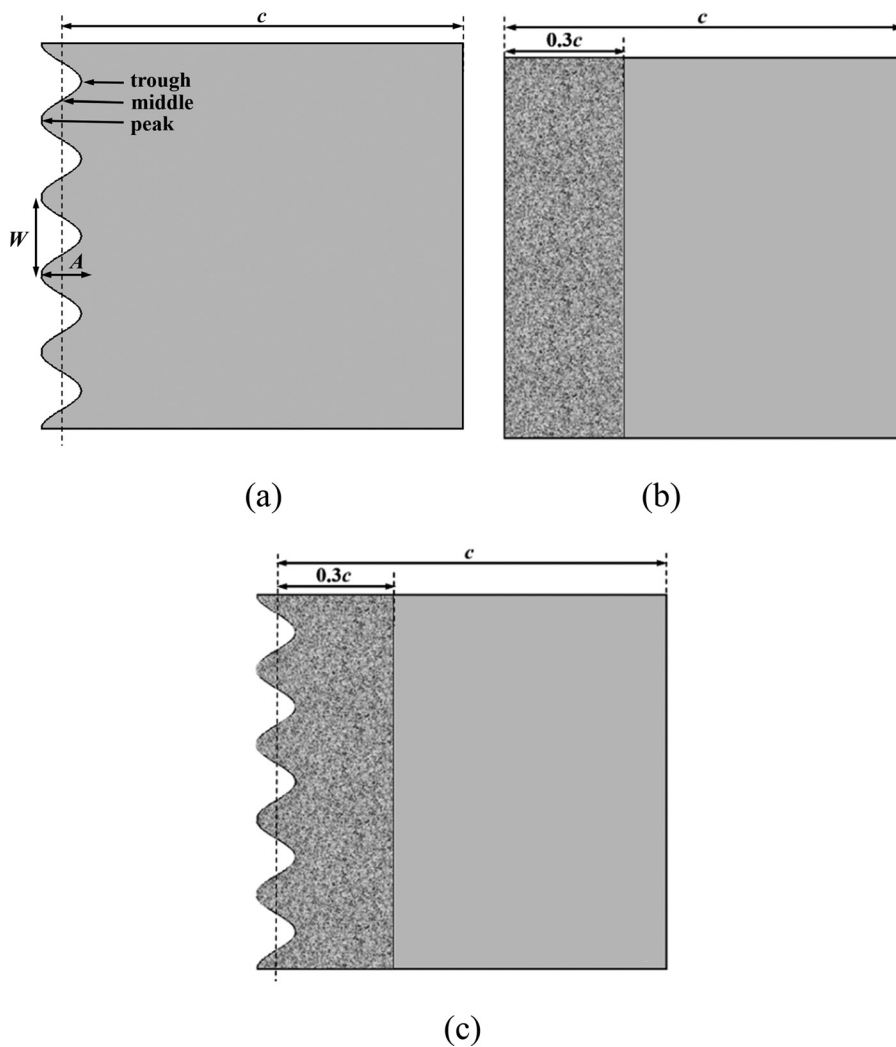


FIG. 1. Sketch of the airfoils with bionic modifications: (a) wavy airfoil, (b) porous airfoil, and (c) poro-wavy airfoil.

amplitude and wavelength are 20% and 10% of the mean chord, respectively. The detailed design method of the wavy leading edges can be found in previous papers of the present authors.<sup>9,13</sup>

The porous treatments are located between the leading edge and 30% of the chord, as shown in Fig. 1(b). The porosity is set to 0.95. The permeability and inertial coefficient are  $1.1 \times 10^{-5}$  and 0.1543, respectively. The poro-wavy airfoil is created by combining the wavy leading edge and the porous leading edge, as shown in Fig. 1(c).

### E. Flow configuration and computational mesh

The tandem rod-airfoil flow configuration is chosen with an airfoil embedded in the wake of a circular rod. This rod-airfoil interaction model has been the subject of many previous studies, as summarized in Table I. The numerical methods, mesh types, mesh nodes/cell numbers, and the extent in the spanwise of the computational domain are given in this table. The URANS,<sup>38,49</sup> scale-adaptive scaling (SAS),<sup>52</sup> detached eddy simulation (DES),<sup>40–43</sup> delayed detached eddy simulation (DDES),<sup>48,50,51,53,54</sup> and large eddy

simulation (LES)<sup>13,39,44–47,55,56</sup> have been used for flow field prediction. Except for the direct noise computation (DNC) method,<sup>43</sup> Amiet's model,<sup>47</sup> and Curle's model,<sup>51</sup> most of the studies utilized the FW-H equation for noise prediction. Both the structured and unstructured mesh have been used for the numerical simulation. Regarding the spanwise length, most of the studies used a length of  $3d$  (where  $d$  is the rod diameter),<sup>39–41,45,47,52,54</sup> while a small length of  $2d$  (Refs. 13, 46, and 55) and long lengths as large as  $30d$  have also been used.<sup>42,43</sup> In a previous study by the present authors, large eddy simulations were conducted with a span of  $2d$  and reasonable results were obtained using a total grid number of  $3.5 \times 10^6$ .<sup>13</sup> In this study, the IDDES method is used with a span of  $3d$ . The resulting grid number is approximately  $7.2 \times 10^6$ , compromising the computational accuracy and efficiency. The first mesh size normal to the wall surface in turbulent units is  $y^+ < 1$ . The present mesh is comparable to previous studies. The predicted aerodynamic and aeroacoustic results are further validated against experimental data and previous studies in the following part.

Figure 2 shows the computational domain and mesh. The airfoil is located  $1c$  downstream the circular rod. The domain extends  $26c$  in



TABLE I. Previous numerical studies on the rod–airfoil configuration.

Year	Authors	Method	Mesh	Nodes/cells	Span
2003	Casalino <i>et al.</i> <sup>38</sup>	URANS + FW-H	2D Structured	$5.4 \times 10^4$	...
2005	Boudet <i>et al.</i> <sup>39</sup>	LES + FW-H	3D Structured	$2.4 \times 10^6$	3 <i>d</i>
2007	Caraeni <i>et al.</i> <sup>40</sup>	DES + FW-H	3D Unstructured	$1.2 \times 10^6$	3 <i>d</i>
2008	Greschner <i>et al.</i> <sup>41</sup>	DES + FW-H	3D Structured	$2.3 \times 10^6$	3 <i>d</i>
2010	Galdéano <i>et al.</i> <sup>42</sup>	DES + FW-H	3D Unstructured	$10 \times 10^6$	30 <i>d</i>
2013	Schell <sup>43</sup>	DES + DNC	3D Structured	$95 \times 10^6$	30 <i>d</i>
2015	Giret <i>et al.</i> <sup>44</sup>	LES + FW-H	3D Unstructured	$5.6 \times 10^6$	3.5 <i>d</i>
2015	Jiang <i>et al.</i> <sup>45</sup>	LES + FW-H	3D Structured	$16 \times 10^6$	3 <i>d</i>
2016	Tong <i>et al.</i> <sup>46</sup>	LES + FW-H	3D Structured	$5.15 \times 10^6$	2 <i>d</i>
2016	Agrawal <i>et al.</i> <sup>47</sup>	LES + Amiet's model	3D Structured	$19 \times 10^6$	3 <i>d</i>
2017	Zhou <i>et al.</i> <sup>48</sup>	DDES + FWH	3D Unstructured	$6 \times 10^6$	3.5 <i>d</i>
2017	Rousoulis <i>et al.</i> <sup>49</sup>	URANS + FW-H	3D Structured	$1.7 \times 10^6$	4.8 <i>d</i>
2018	Chen <i>et al.</i> <sup>13</sup>	LES + FW-H	3D Structured	$3.5 \times 10^6$	2 <i>d</i>
2019	Sharma <i>et al.</i> <sup>50</sup>	DDES + FW-H	2D Unstructured	$4 \times 10^6$	...
2019	Samion <i>et al.</i> <sup>51</sup>	DDES + Curle's model	3D Structured	$3 \times 10^6$	3.5 <i>d</i>
2020	Li <i>et al.</i> <sup>52</sup>	SAS + FW-H	3D Structured	$3 \times 10^6$	3 <i>d</i>
2020	Jin <i>et al.</i> <sup>53</sup>	DDES + FW-H	3D Structured	$7 \times 10^6$	3 <i>d</i>
2021	Sharma <i>et al.</i> <sup>54</sup>	DDES + FW-H	3D Unstructured	$110 \times 10^6$	3 <i>d</i>
2022	Yang <i>et al.</i> <sup>55</sup>	LES + FW-H	3D Structured	$5.58 \times 10^6$	2 <i>d</i>
2023	Han <i>et al.</i> <sup>56</sup>	LES + FW-H	3D Structured	$8.3 \times 10^6$	7 <i>d</i>
2024	Present study	IDDES + FW-H	3D Structured	$7.2 \times 10^6$	3 <i>d</i>

the streamwise direction,  $20c$  in the cross-stream direction, and  $0.3c$  in the spanwise direction. The rod diameter  $d$  is 15 mm and the airfoil chord  $c$  is 150 mm. The blue line represents the location of the permeable FW-H surface, which is similar to the study of Jiang *et al.*,<sup>45</sup> Han *et al.*,<sup>56</sup> Zhou *et al.*,<sup>57</sup> and Zhu *et al.*<sup>58</sup> The mesh around the rod and baseline airfoil is plotted in Fig. 2(b). There are 304 grid nodes around the rod and 530 grid nodes around the airfoil. For the baseline and porous airfoils, there are 31 uniform grid nodes along the span, leading to a total grid node of  $7.2 \times 10^6$  and  $7.6 \times 10^6$  in the whole domain, respectively. For the wavy and poro-wavy airfoils, the spanwise grid number is refined to 43, leading to a total grid node of  $10.2 \times 10^6$  and  $10.9 \times 10^6$  in the whole domain, respectively. The mesh on the baseline and wavy airfoils are shown in Figs. 2(c) and 2(d).

The velocity inlet and pressure outlet boundary conditions are imposed at the inlet and outlet, respectively. An adiabatic no-slip condition is imposed on the rod and airfoil surfaces. The periodicity boundary condition is used in the spanwise direction. The inflow velocity is 40 m/s with an angle of attack of  $0^\circ$ , and the outlet pressure is set to 96 400 Pa. The chord-based Reynolds number is approximately 400 000. The pressure-velocity coupling is solved using the semi-implicit method for pressure-linked equations-consistent (SIMPLEC) algorithm. The convection and diffusion terms are discretized using a bounded central differencing scheme. A bounded second-order implicit scheme is used for time marching. The computation time step is  $1 \times 10^{-5}$  s, and the total acquired time for acoustic processing is 0.1 s. A Hanning window with a block-size of 1024 data is used to compute the spectra using Welch's method,<sup>59</sup> and the data overlap is 50%.

## F. Validation of the numerical method

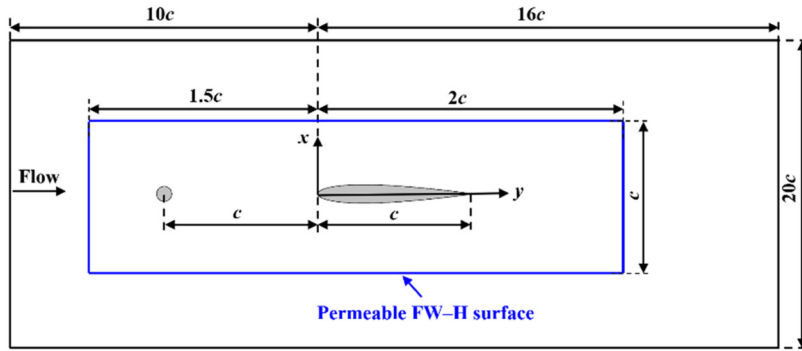
In this paper, the streamwise velocity in the rod wake is measured by a single hot wire. The detailed experimental setup can be found in the previous paper of the present authors.<sup>9</sup> The computed mean velocity and fluctuation velocity in the rod wake ( $x = -0.25c$ ) are compared against the experimental data in Fig. 3. It can be found that the predicted values agree well with the experiments. The two peaks in the fluctuation velocity are also well captured with a slight underprediction of the fluctuation velocity.

The time-averaged pressure coefficient and fluctuation pressure coefficient are defined by

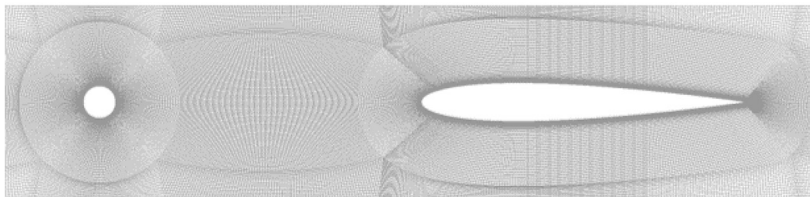
$$C_p = \frac{\langle p \rangle - p_0}{0.5\rho_0 U_0^2}, \quad (13)$$

$$C'_p = \frac{p'_{rms}}{0.5\rho_0 U_0^2}, \quad (14)$$

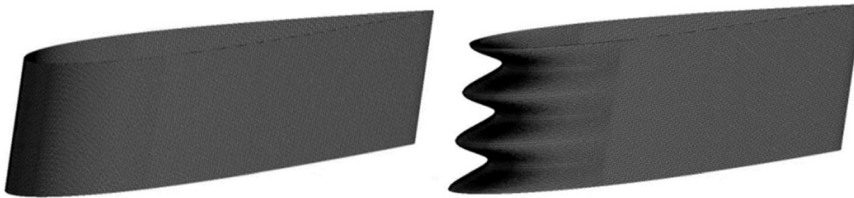
where  $\langle p \rangle$  is the mean pressure on the airfoil surface,  $p_0$  is the free-field pressure,  $\rho_0$  is the free-field density,  $U_0$  is the free-field velocity, and  $p'_{rms}$  is the rms value of the fluctuating pressure. The computed negative pressure coefficient and fluctuation pressure coefficient on the baseline airfoil surface are plotted in Fig. 4, together with the LES results of Giret *et al.*<sup>44</sup> and the LES results of Boudet.<sup>60</sup> The mean pressure distributions are in good agreement with the data of Giret *et al.*, and they collapse with Boudet's data up to  $x = 0.9c$ . Regarding the fluctuation pressure distributions, they yield excellent agreement with the data of Giret *et al.* except for the exact leading edge. The slight discrepancy between the pressure side and suction side in the present study



(a)



(b)



(c)

(d)

FIG. 2. Computational domain and mesh: (a) computational domain, (b) mesh around the rod and baseline airfoil, (c) mesh on the baseline airfoil, and (d) mesh on the wavy airfoil.

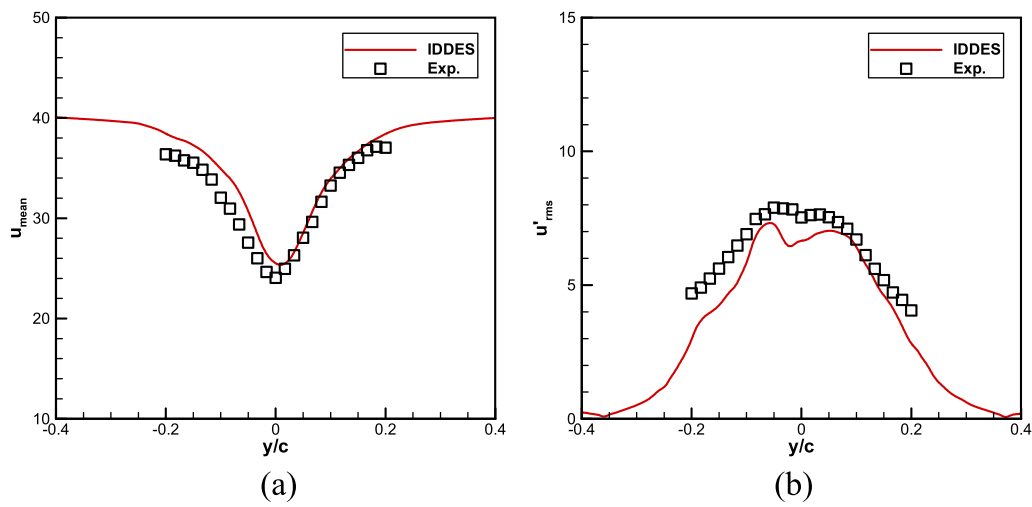


FIG. 3. Profiles of the streamwise mean velocity and fluctuation velocity in the rod wake: (a) mean velocity and (b) fluctuation velocity.

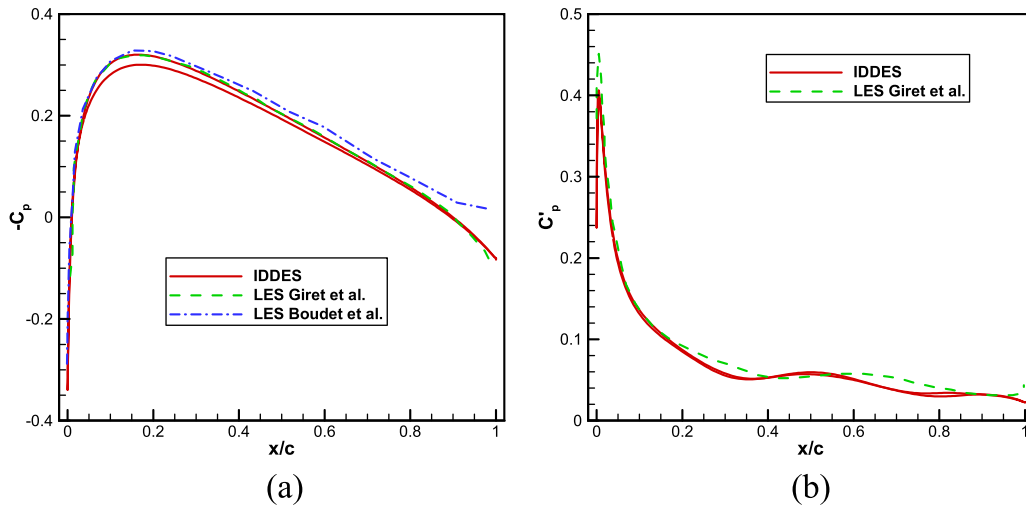


FIG. 4. Distributions of the mean and fluctuation pressure on the airfoil surface: (a) mean pressure and (b) fluctuation pressure.

might be due to a lack of time series, resulting in poorly converged statistics.<sup>13</sup>

The far-field noise of the rod-airfoil configuration has been measured by the present authors, and the experimental data are used for validation of the predicted aeroacoustic results.<sup>9</sup> The far-field sound pressure level (SPL) is defined by

$$\text{SPL}(f) = 10 \log_{10} \left( S_{pp}(f) / p_{ref}^2 \right), \quad (15)$$

where  $S_{pp}(f)$  is the auto-spectrum of the sound pressure,  $p_{ref} = 2 \times 10^{-5}$  Pa is the reference pressure.

Regarding the comparison between the numerical and experimental data, spanwise corrections should be performed because the spanwise lengths in the numerical simulation (3d) and experiment (20d) are different. An extended aeroacoustic spanwise correction method that can account for the frequency-dependent coherence length has been proposed by the present authors. The spanwise SPL correction equation is as follows:<sup>61</sup>

$$\Delta \text{SPL}(f) = 10 \log_{10} \frac{\exp\left(-\frac{\pi L_{exp}^2}{4 L_c^2}\right) + \frac{\pi L_{exp}}{2 L_c} \text{erf}\left(\frac{\sqrt{\pi} L_{exp}}{2 L_c}\right) - 1}{\exp\left(-\frac{\pi L_{sim}^2}{4 L_c^2}\right) + \frac{\pi L_{sim}}{2 L_c} \text{erf}\left(\frac{\sqrt{\pi} L_{sim}}{2 L_c}\right) - 1}, \quad (16)$$

where  $L_{exp}$  and  $L_{sim}$  are the spanwise extent in the experiment and numerical simulation, respectively.  $L_c$  is the frequency-dependent spanwise coherence length of the fluctuating pressure, and  $\text{erf}(\cdot)$  is the error function.

The SPL spectra are computed on a circle centered at the mid-span mid-chord point of the airfoil with a radius of 1.5 m. The permeable FW-H surface is used for the prediction of the far-field noise. The predicted sound spectra and directivity patterns are compared to the measured data in Fig. 5. The directivity angles are defined relative to

the downstream direction of the airfoil. It is found that the predicted results agree well with the measured data at all the directivity angles, and both the tonal noise and broadband noise are well captured. The overall sound pressure level (OASPL) shown in Fig. 5(d) is computed by integrating the spectra from 100 to 10 000 Hz. The rod-airfoil interaction noise exhibits a dipole sound source, and the predicted values are in excellent agreement with the experimental data.

### III. RESULTS AND DISCUSSION

#### A. Effects of bionic treatments on the aerodynamic performance

The time history of the lift and drag coefficients for the baseline and bionic airfoils are plotted in Fig. 6. The lift coefficient and drag coefficient are defined by

$$C_L = \frac{F_L}{0.5 \rho_0 U_0^2 S}, \quad (17)$$

$$C_D = \frac{F_D}{0.5 \rho_0 U_0^2 S}, \quad (18)$$

where  $F_L$  is the lift,  $F_D$  is the drag, and  $S$  is the projected area of the airfoil, which is the same for the baseline and bionic airfoils.

It can be seen from Fig. 6(a) that the bionic airfoils have a negligible effect on the mean lift, but the lift fluctuations are significantly reduced by the bionic airfoils, especially for the poro-A20W10 airfoil. As shown in Fig. 6(b), the mean drag is slightly increased by the A20W10 airfoil, but it is considerably increased by the bionic airfoils with porous treatments. The drag fluctuations are also reduced by the bionic treatments.

The power spectral density (PSD) of the fluctuating lift and drag for the baseline and bionic airfoils are compared in Fig. 7. It is found that the lift fluctuations are more intensive than the drag fluctuations for all the airfoils. According to Curle's acoustic analogy theory,<sup>62</sup> on the hypothesis of acoustic and geometric far-field and compact noise source, the far-field sound pressure can be simplified as



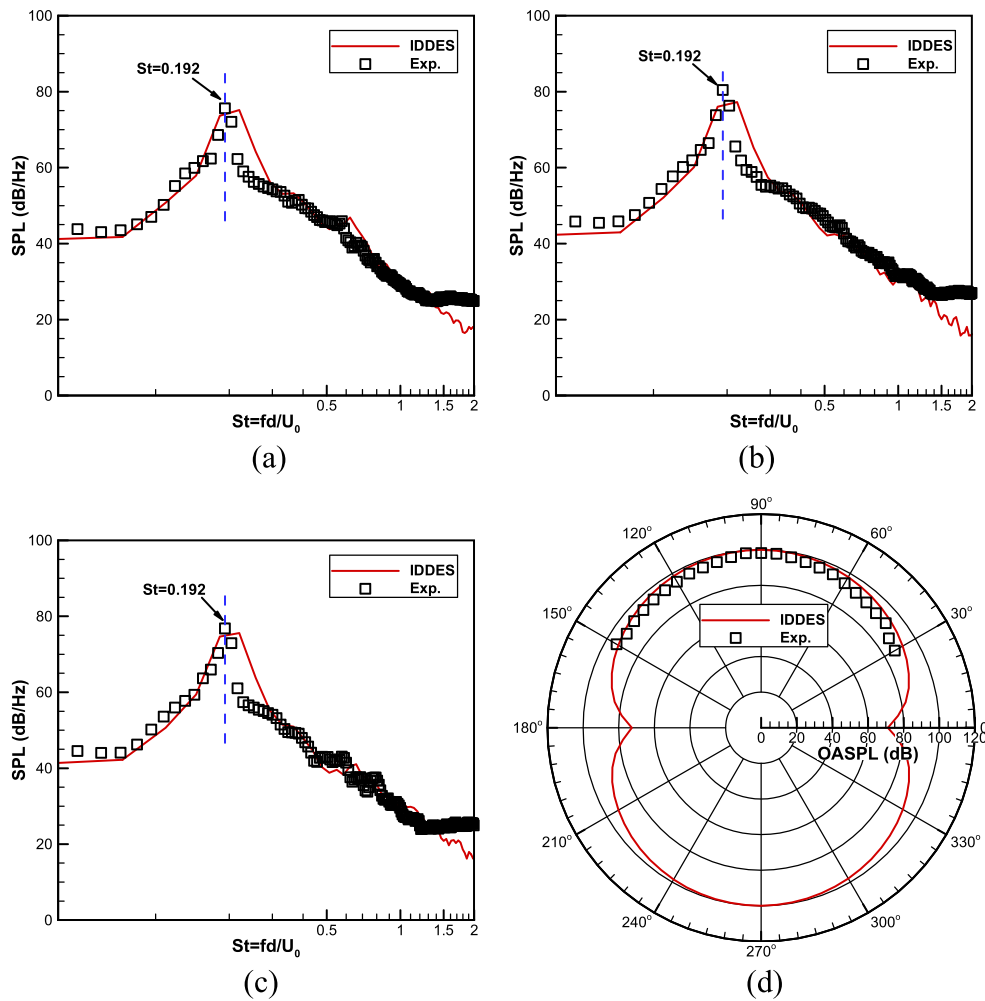


FIG. 5. Comparison of the predicted far-field SPL and directivity pattern with the experiments: (a) SPL at  $\theta = 60^\circ$ , (b) SPL at  $\theta = 90^\circ$ , (c) SPL at  $\theta = 120^\circ$ , and (d) OASPL.

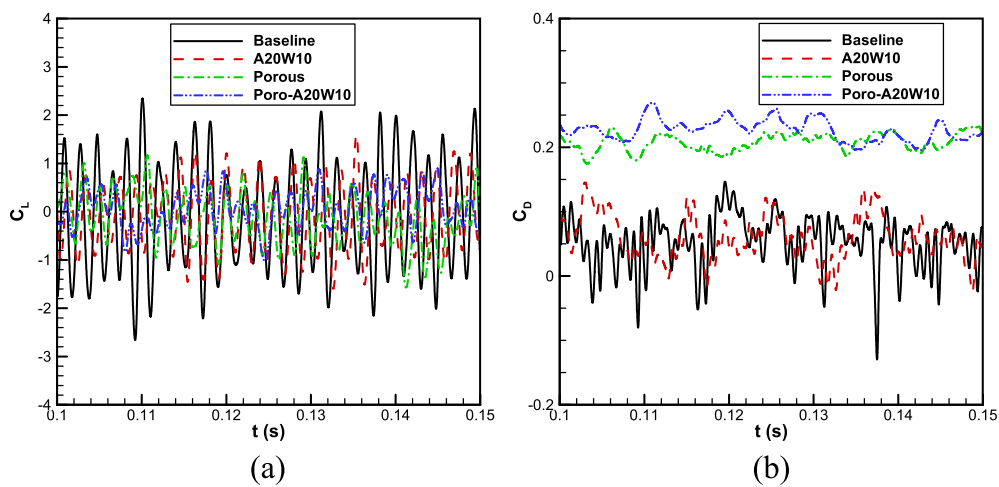


FIG. 6. Time history of the lift and drag coefficients for the baseline and bionic airfoils: (a) lift coefficient and (b) drag coefficient.

09 April 2024 10:28:22

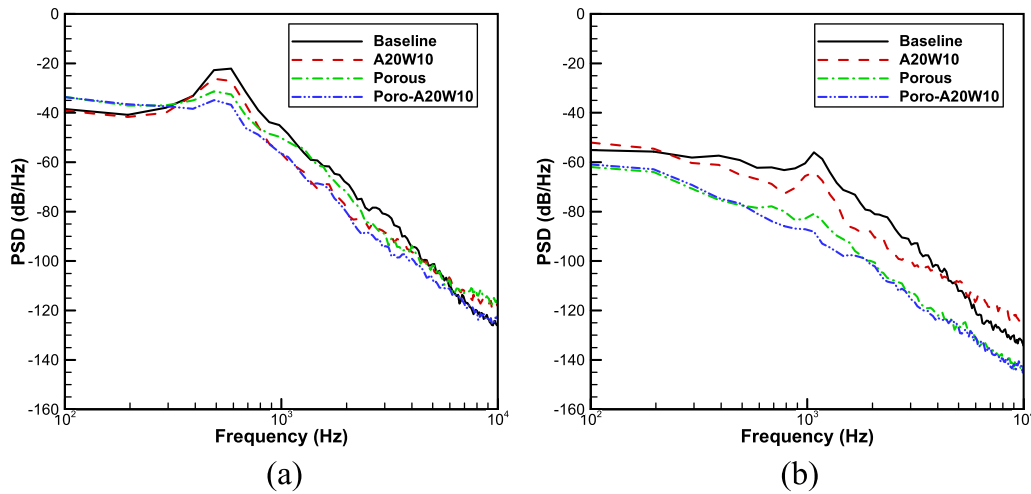


FIG. 7. Power spectral density of the lift and drag coefficients for the baseline and bionic airfoils: (a) lift coefficient and (b) drag coefficient.

$$p'(\mathbf{x}, t) = \frac{1}{4\pi c_0} \frac{x_i}{x^2} \frac{\partial}{\partial t} F_i(t), \quad (19)$$

where  $F_i(t)$  is the total resultant force exerted upon the fluid by the solid boundaries. The fluctuation force  $F_i(t)$  can be divided into fluctuation lift  $F_L(t)$  and fluctuation drag  $F_D(t)$ . It can be seen from Eq. (19) that the far-field sound is generally proportional to the fluctuation lift and drag. The results plotted in Fig. 7 indicate that the lift noise generated by the fluctuation lift is much larger than the drag noise generated by the fluctuation drag for all the airfoils.

As shown in Fig. 7(a), in the low-frequency range below 300 Hz, the lift fluctuation is slightly increased by the porous and poro-A20W10 airfoils, while the A20W10 airfoil has comparable value with the baseline airfoil. Around the vortex shedding frequency of 488 Hz, all the three bionic treatments can significantly reduce the lift fluctuations. The A20W10 airfoil obtains the least reduction, while the poro-A20W10 achieves the best reduction. In the middle frequency range between 1000 and 3000 Hz, the porous airfoil has a weak reduction effect, while the A20W10 and poro-A20W10 obtain a better reduction level. In the high-frequency range above 6000 Hz, the lift fluctuations are increased by the A20W10 and porous airfoils. Regarding the drag fluctuations shown in Fig. 7(b), they are reduced in almost the whole frequency range except for the A20W10 airfoil at high frequencies. The different bionic treatments affect the turbulence-airfoil interaction in different ways. The wavy leading edges act as vortex generators that can induce streamwise vortices interacting with the incoming turbulence. The porous materials act as soft boundary that can release pressure fluctuations and can also induce small-scale turbulence. The low-frequency increase in the lift fluctuations for the porous and poro-A20W10 airfoils is conjectured to be mainly due to the flow separation at the junction of porous and solid parts, while the high-frequency increase in lift fluctuations for the A20W10 and porous airfoils might be due to the small-scale turbulence induced by the bionic treatments.

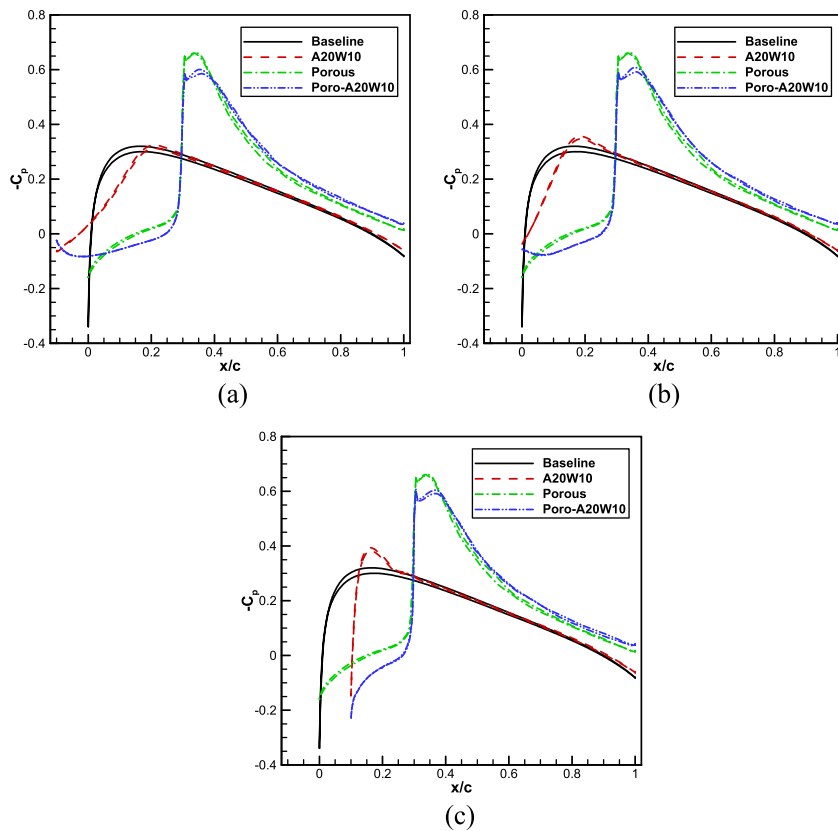
The mean and rms values of the lift and drag coefficients for the baseline and bionic airfoils are summarized in Table II. It is straightforward that the bionic airfoils are detrimental to the mean drag, especially for the airfoils with porous materials. The mean drag is increased

TABLE II. Comparison of the aerodynamic force of the baseline and bionic airfoils.

Airfoil	$\bar{C}_D$	$C'_{D,rms}$	$C'_{L,rms}$
Baseline	0.0473	0.0444	1.1593
A20W10	0.0608	0.0385	0.7236
Porous	0.2062	0.0124	0.5342
Poro-A20W10	0.2248	0.0142	0.4472

by 28.5%, 335.9%, and 375.3% by the A20W10, porous, and poro-A20W10 airfoils, respectively. The flow on the bionic airfoils is more complicated than that on the smooth baseline airfoil. Flow mixing and momentum exchange are increased for the bionic airfoils, which enhance flow losses. A low-pressure region with large velocity deficit in the airfoil wake is found for the bionic airfoils, as can be seen in the following Fig. 9. The pressure drag is thought to be the main reason for the overall drag increase. However, the lift and drag fluctuations are significantly reduced by the bionic airfoils. The drag fluctuations are reduced by 13.3%, 72.1%, and 68%, while the lift fluctuations are reduced by 37.6%, 53.9%, and 61.4% by the A20W10, porous, and poro-A20W10 airfoils, respectively. As discussed in Eq. (19), the lift and drag fluctuations are good indicators of the propagated sound. The reduced lift and drag fluctuations contribute a lot to the far-field noise reduction.<sup>62-64</sup>

Figure 8 shows the mean pressure distributions at the peak location, middle location, and trough location of the baseline and bionic airfoils. The spanwise sections of the peak, middle, and trough are depicted in Fig. 1(a). It can be observed from Fig. 8 that the A20W10 airfoil has only obvious influence on the mean pressure in the leading-edge region of the airfoil before  $x = 0.3c$ , while it exerts negligible effect from  $x = 0.3c$  on the airfoil trailing edge. A low-pressure region is observed behind the trough of the A20W10 airfoil. For the porous and poro-A20W10 airfoils, very different mean pressure distributions are observed. A very low-pressure region is found at the junction of the porous materials and solid body, and the low-pressure maintains up to the airfoil trailing edge.



**FIG. 8.** Comparison of the mean pressure at different spanwise locations of the airfoils: (a) peak location, (b) middle location, and (c) trough location.

The effects of the three bionic treatments on the mean streamwise velocity in the airfoil wake ( $x = 1.1c$ ) are shown in Fig. 9. The results show that the wake velocity deficits are slightly enhanced by the A20W10 airfoil, while they are significantly increased by the porous and poro-A20W10 airfoils. The wake is also much widened by the two porous airfoils. The effects of the bionic airfoils on the fluctuating streamwise velocity in the airfoil wake ( $x = 1.1c$ ) are further plotted in Fig. 10. Similar to the mean velocity distributions, the fluctuating velocity is slightly increased by the A20W10 airfoil, while it is increased a lot by the two porous airfoils, especially for the poro-A20W10 airfoil. It is conjectured that the porous part of the airfoil introduces more surface roughness and cross-flow, resulting in a thickened boundary layer and widened wake. It can also be seen from Figs. 9 and 10 that there are no obvious differences at the peak, middle, and trough locations for each airfoil.

## B. Noise reduction effects of the bionic treatments

In this subsection, in order to focus on the noise reduction effects of the bionic modifications, the airfoil surfaces are chosen as the sound source to remove the influence of the rod on the noise spectra. The far-field SPL spectra for the baseline and bionic airfoils are compared in Fig. 11 at different directivity angles of  $\theta = 30^\circ, 60^\circ, 90^\circ,$  and  $120^\circ$ . The results indicate that, in the very low-frequency range below 300 Hz, the A20W10 airfoil has negligible effects on the noise spectra, while the noise is slightly increased by the porous and poro-A20W10

airfoils. Around the vortex shedding frequency, the tonal noise is significantly reduced by all the three bionic treatments. Compared to the wavy A20W10 airfoil, the porous airfoil obtains more tonal noise reduction, while the combined poro-wavy airfoil achieves further greater tonal noise reduction. The underlying mechanisms for noise reduction of the different bionic treatments are discussed in Sec. III C.

In the mid- to high-frequency range, the broadband noise is also considerably reduced by the bionic treatments. Unlike the tonal noise, the A20W10 airfoil is more effective for broadband noise reduction, compared to the porous airfoil, while the combined poro-wavy airfoil can obtain more broadband noise reduction. In the high-frequency range, the noise is increased by all the three bionic airfoils. However, the combined poro-wavy airfoil has comparable noise level with the A20W10 airfoil, which is much lower than that of the porous airfoil. In general, the poro-wavy airfoil is found to have both the advantages of the wavy airfoil and porous airfoil. The poro-wavy airfoil can not only significantly reduce the tonal noise but also the broadband noise. At the directivity angle of  $90^\circ$ , the tonal noise is reduced by 4.6, 10.2, and 12.2 dB by the A20W10, porous, and poro-A20W10 airfoils, respectively, while the broadband noise can be decreased by up to 10 dB by the poro-A20W10 airfoil.

The directivity patterns of the baseline and bionic airfoils, together with the corresponding OASPL reduction level are shown in Fig. 12. The OASPL reduction level is calculated by the OASPL of the baseline airfoil minus the OASPL of the bionic airfoil. Positive values of the OASPL reduction level represent a noise reduction effect of the

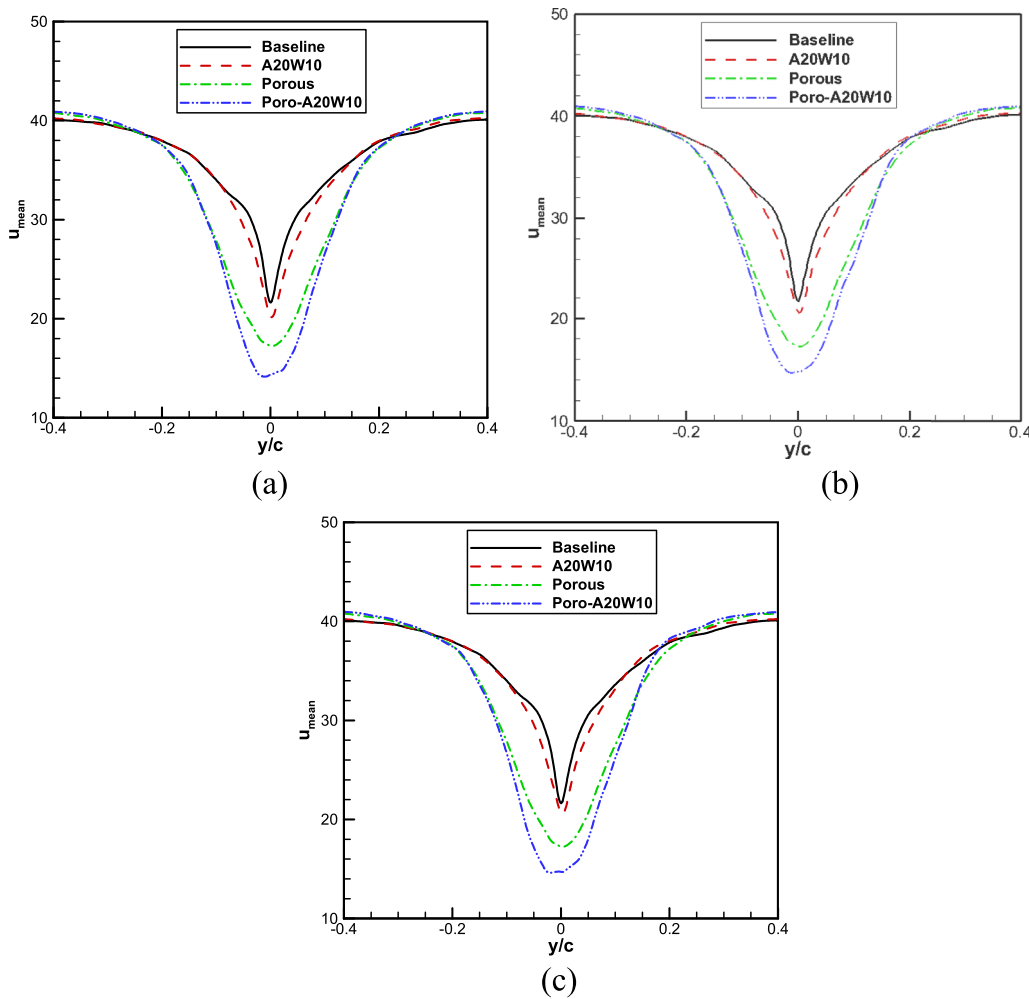


FIG. 9. Comparison of the mean streamwise velocity in the airfoil wake at different spanwise locations: (a) peak location, (b) middle location, and (c) trough location.

bionic treatment, while negative values indicate a noise amplification effect. The integrated frequency range of OASPL is between 100 and 10 000 Hz since humans are not sensitive to the noise in the very low and very high-frequency range. The directivity patterns generally exhibit dipole sound source for all the baseline and bionic airfoils. The OASPL is reduced by all the three bionic treatments. The wavy A20W10 airfoil obtains the least noise reduction, followed by the porous airfoil, while the combined poro-wavy airfoil achieves the best noise reduction effect. At the directivity angle of  $90^\circ$ , the OASPL is reduced by 4.4, 8.8, and 11.5 dB by the A20W10, porous, and poro-A20W10 airfoils, respectively.

The OASPL reduction levels are compared to the force fluctuation reduction in Table III. The used force fluctuations are shown in Table II. Both the solely lift fluctuation and the summation of lift fluctuation and drag fluctuation are computed, and the results show no difference because the drag fluctuation is much lower than the lift fluctuation. The force fluctuation reduction is 4.1, 6.7, and 8.3 dB for the A20W10, porous, and poro-A20W10 airfoils, respectively. The force

fluctuation reduction level is comparable but lower than that of the OASPL reduction level, which suggests that the reduction of the unsteady force is not the only noise reduction mechanism of the bionic treatments.

### C. Noise reduction mechanisms of the bionic treatments

In this subsection, the noise reduction mechanisms of the different bionic treatments are discussed in detail. Following Amiet's leading-edge noise model, the PSD of the far-field sound pressure can be written as follows:<sup>1</sup>

$$S_{pp}(x, y, 0, \omega) = \left( \frac{\omega y \rho_0 b M}{\sigma^2} \right)^2 d |\ell(x, K_x, 0)|^2 l_z(\omega) S_{ww}(\omega), \quad (20)$$

where  $\sigma = \sqrt{x^2 + \beta^2(y^2 + z^2)}$ ,  $\beta = \sqrt{1 - M^2}$ , and  $M$  is the flow Mach number.  $b$  and  $d$  are the semi-chord and semi-span of the airfoil,

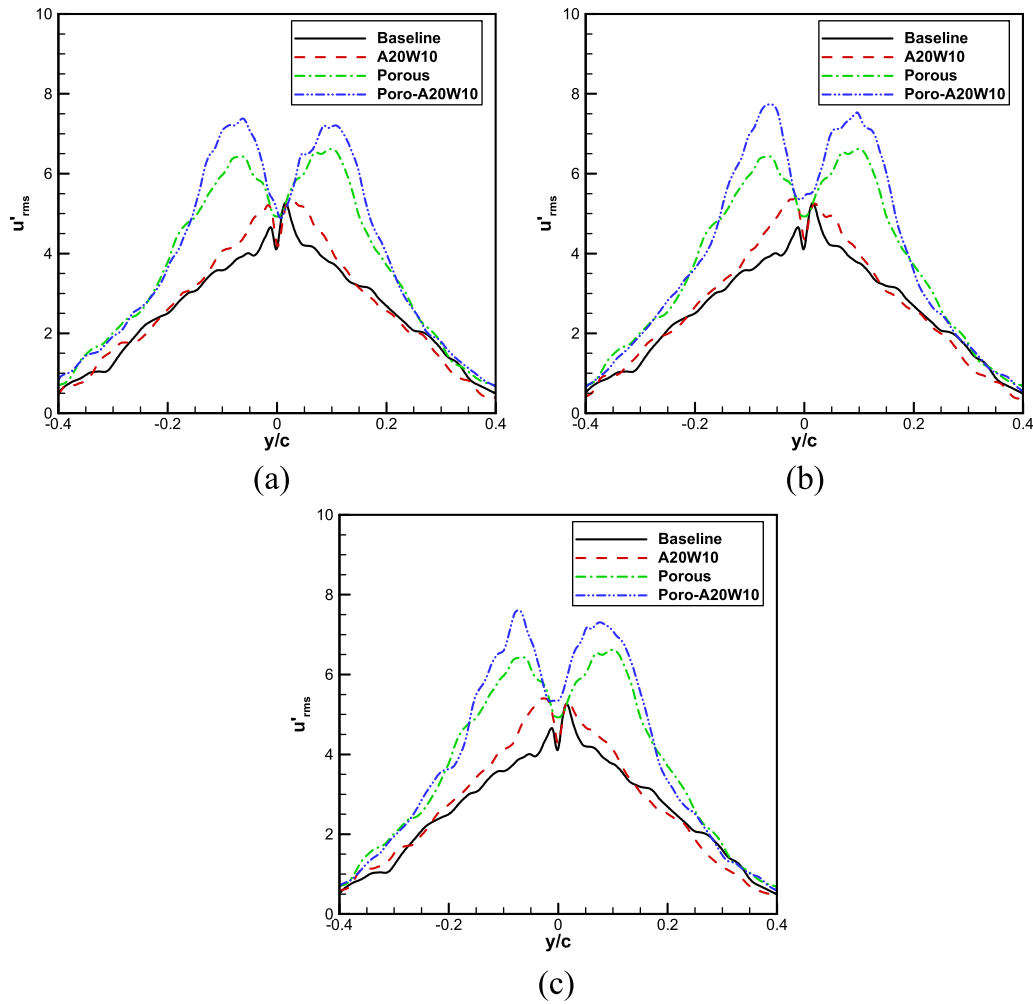


FIG. 10. Comparison of the fluctuating streamwise velocity in the airfoil wake at different spanwise locations: (a) peak location, (b) middle location, and (c) trough location.

respectively.  $\ell$  is the integral of airfoil pressure distribution,  $K_x$  is the chordwise turbulence wavenumber.  $l_z(\omega)$  is the frequency-dependent spanwise coherence length of turbulence, and  $S_{wv}(\omega)$  is the PSD of the vertical velocity fluctuations. It can be found that, the far-field sound level is proportional to the sound source intensity and spanwise coherence of the turbulence. Therefore, noise reduction can be achieved by either reducing the sound source intensity or the spanwise coherence level.

The fluctuating pressure on the airfoil surface is a good indicator of the sound source intensity. The root mean square error (rmse) of the pressure, which equals to the rms value of the fluctuating pressure is plotted in Fig. 13 for the baseline and bionic airfoils. It is noticed that, for the baseline airfoil, intensive pressure fluctuations are mainly located at the leading-edge region and are uniformly distributed along the span. For the wavy A20W10 airfoil as shown in Fig. 13(b), intensive pressure fluctuations are only observed in the trough region, while they are considerably reduced in the peak and middle regions. The porous airfoil plotted in Fig. 13(c) exhibits more distinct characteristics. The

intensive pressure fluctuations along the leading edge are totally removed, while large pressure fluctuations are found around the junction of the porous part and solid part of the airfoil. As shown in Fig. 13(d), for the poro-A20W10 airfoil, both the pressure fluctuations along the leading edge and at the junction region are significantly reduced, which means that the poro-A20W10 airfoil has both the advantages of the wavy modification and porous treatment.

The pressure fluctuations on the spanwise middle planes are further plotted in Fig. 14 for the baseline and bionic airfoils. It is apparent that the pressure fluctuations are mainly located nearby the airfoil for all the four airfoils. For the baseline and A20W10 airfoils, the pressure fluctuations are observed at the leading-edge region, but they are significantly reduced for the A20W10 airfoil. For the porous and poro-A20W10 airfoils, the pressure fluctuations are induced at the junction of the porous part and solid part, but they are much lower for the combined poro-A20W10 airfoil. However, compared to the baseline airfoil, the pressure fluctuations behind the junction are increased for the two airfoils with porous treatments. The pressure fluctuation distributions



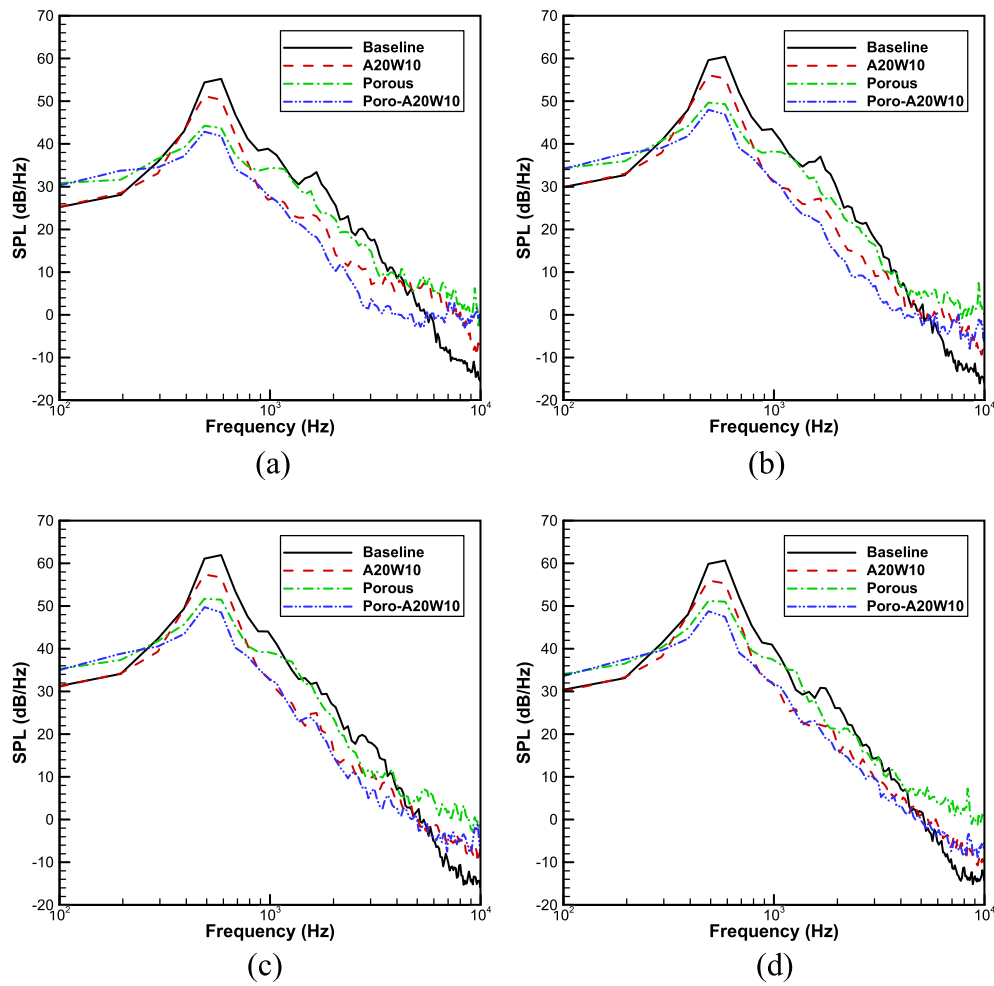


FIG. 11. Comparison of the predicted SPL of the baseline and bionic airfoils at different directivity angles: (a)  $\theta = 30^\circ$ , (b)  $\theta = 60^\circ$ , (c)  $\theta = 90^\circ$ , and (d)  $\theta = 120^\circ$ .

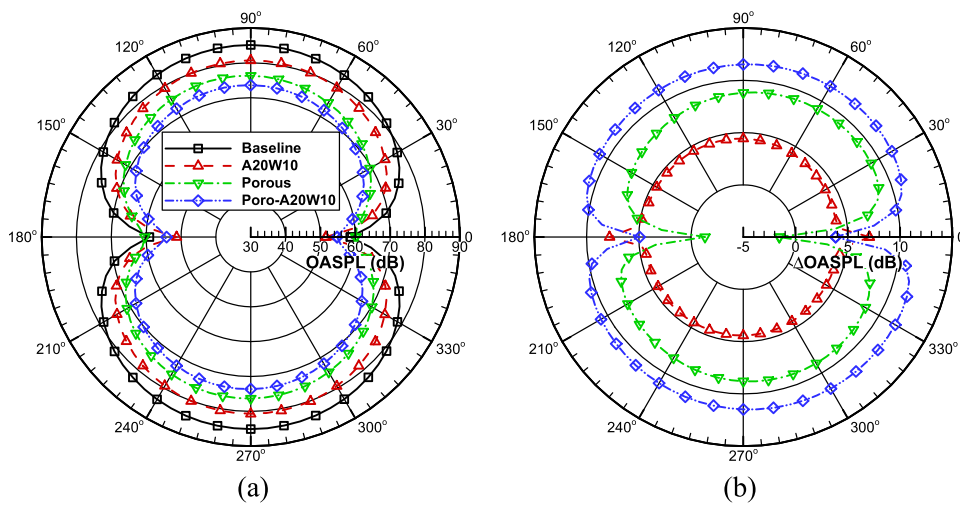


FIG. 12. Comparison of the predicted OASPL of the baseline and bionic airfoils and the corresponding OASPL reduction level: (a) OASPL and (b) OASPL reduction.

09 April 2024 10:28:22

TABLE III. Comparison between the force fluctuation reduction and the OASPL reduction for the three bionic treatments.

Airfoil	$10 \log_{10} \frac{(C_{L,rms}^2)_{Baseline}}{(C_{L,rms}^2)_{Bionic}} \text{ (dB)}$	$10 \log_{10} \frac{(C_{L,rms}^2 + C_{D,rms}^2)_{Baseline}}{(C_{L,rms}^2 + C_{D,rms}^2)_{Bionic}} \text{ (dB)}$	$\Delta\text{OASPL (dB)}$
A20W10	4.1	4.1	4.4
Porous	6.7	6.7	8.8
Poro-A20W10	8.3	8.3	11.5

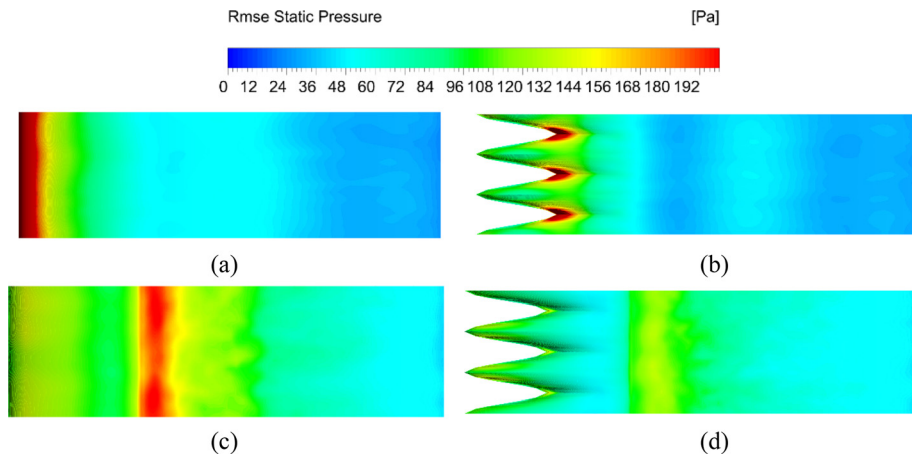


FIG. 13. Comparison of the pressure fluctuations on the airfoil surface: (a) baseline, (b) A20W10, (c) porous, and (d) poro-A20W10.

at the peak and trough locations exhibit similar characteristics and are not shown for clarity.

The chordwise pressure fluctuations at different spanwise locations are depicted in Fig. 15 for the baseline and bionic airfoils. For the

baseline airfoil, large pressure fluctuations are observed from the leading edge till the 30% chord. Then the pressure fluctuations maintain at a low level up to the airfoil trailing edge. These phenomena confirm the rationality of using porous treatments from the leading edge to the

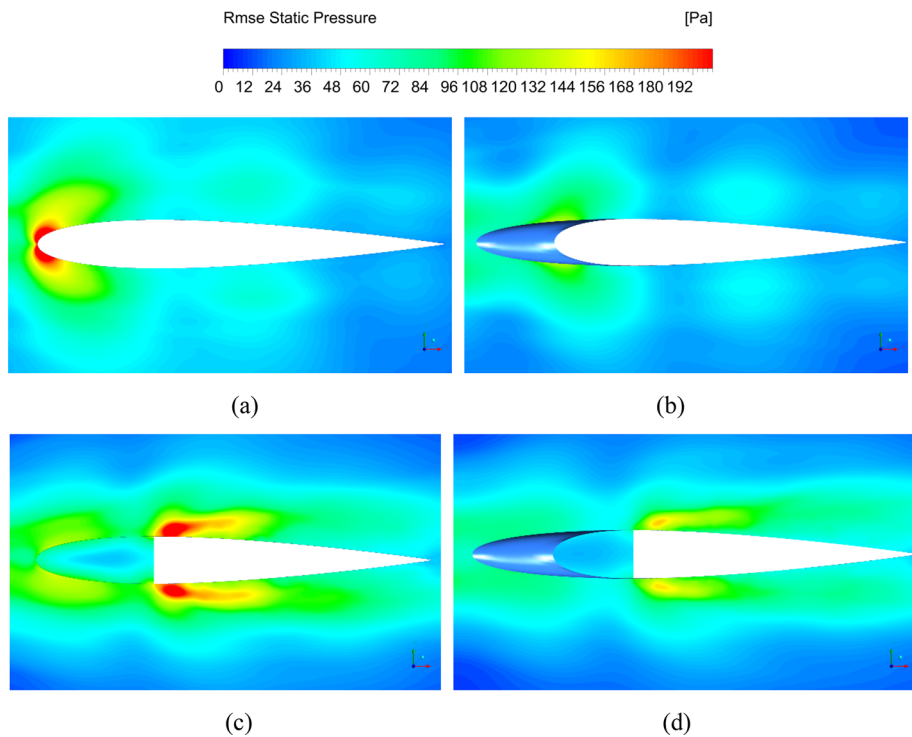


FIG. 14. Comparison of the pressure fluctuations on the spanwise middle planes: (a) baseline, (b) A20W10, (c) porous, and (d) poro-A20W10.

09 April 2024 10:28:22

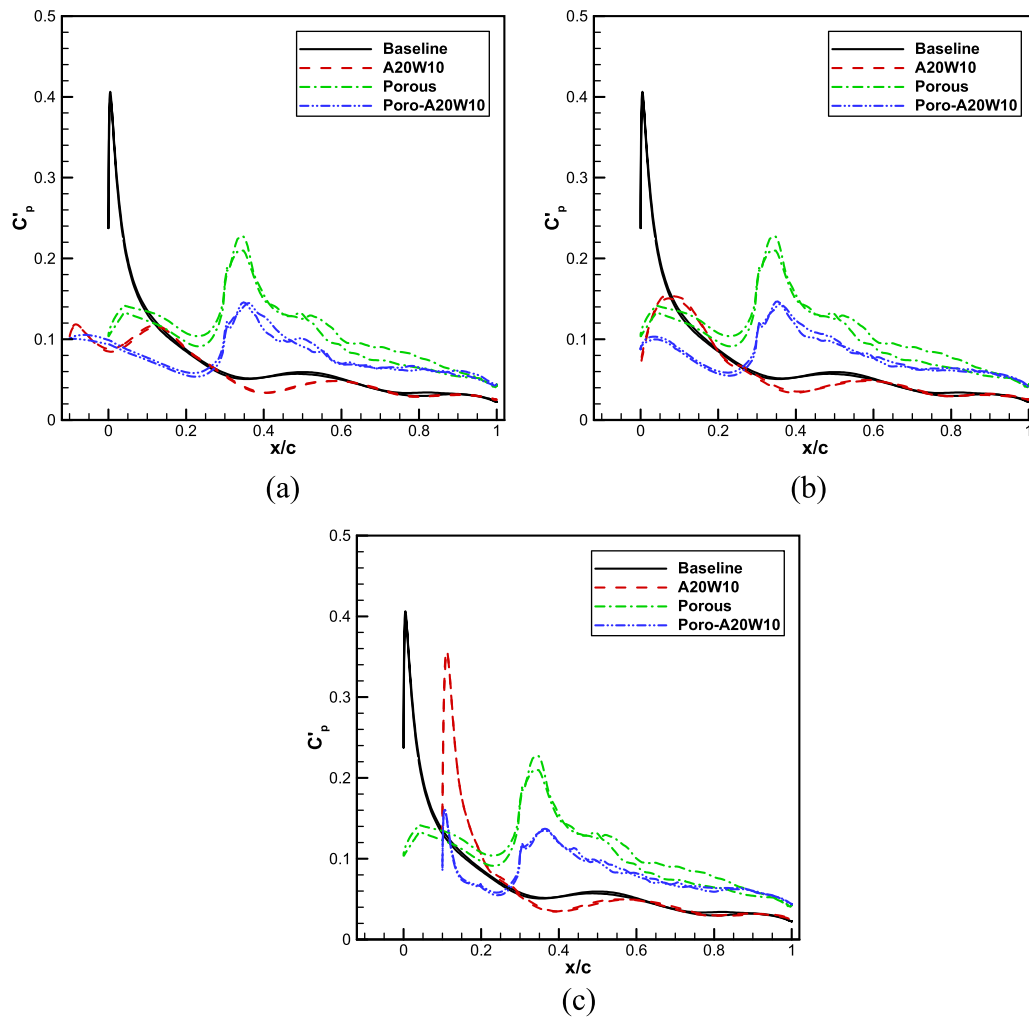


FIG. 15. Chordwise pressure fluctuations at different spanwise locations of the airfoils: (a) peak location, (b) middle location, and (c) trough location.

30% chord. For the A20W10 airfoil, much lower pressure fluctuations are found in the leading-edge region except for the trough location. From 30% chord to the airfoil trailing-edge, the A20W10 airfoil has comparable pressure fluctuations with the baseline airfoil. For the porous airfoil, the pressure fluctuations are significantly reduced in the leading-edge region, and the sound source is much lower at the trough location compared to the A20W10 airfoil. Very intensive pressure fluctuations appear at 30% chord for the porous airfoil at the junction of porous and solid parts. The poro-A20W10 airfoil achieves the lowest pressure fluctuations along the whole airfoil surface, which contribute a lot to its lowest noise radiation. However, in the rear part of the airfoil, the pressure fluctuations are increased by the porous airfoil and poro-A20W10 airfoil.

In order to examine the reason for the increased pressure fluctuations at the junction of the porous and solid parts for the two airfoils with porous treatments, the time-averaged streamlines on the middle planes are plotted in Fig. 16 for the baseline and bionic airfoils. The streamlines are colored by the mean velocity. For the baseline and

A20W10 airfoils, the flow goes smoothly around the airfoil. However, for the porous and poro-A20W10 airfoils, flow separation occurs at the junction of the porous and solid parts, resulting in intensive pressure fluctuations.

The flow separation at the junction of the porous and solid parts will affect the flow at the last 70% part of the airfoils. The far-field sound radiated by the first 30% part and the last 70% part of the baseline and bionic airfoils are compared in Fig. 17. As shown in Fig. 17(a), the noise generated by the first 30% part of the airfoil is reduced by all the three bionic treatments except for the high-frequency noise above 6000 Hz. One of the most important findings from Fig. 17(b) is that, the flow separation at the junction of the porous and solid parts can significantly increase the low-frequency noise below 400 Hz. A study using a streamlined connection between the porous part and solid part is ongoing to eliminate the flow separation, which is thought to be able to further enhance the noise reduction level of the combined poro-wavy treatments.

The spanwise averaged auto- and cross-power spectral density of the fluctuating pressure at the airfoil leading edge is compared in

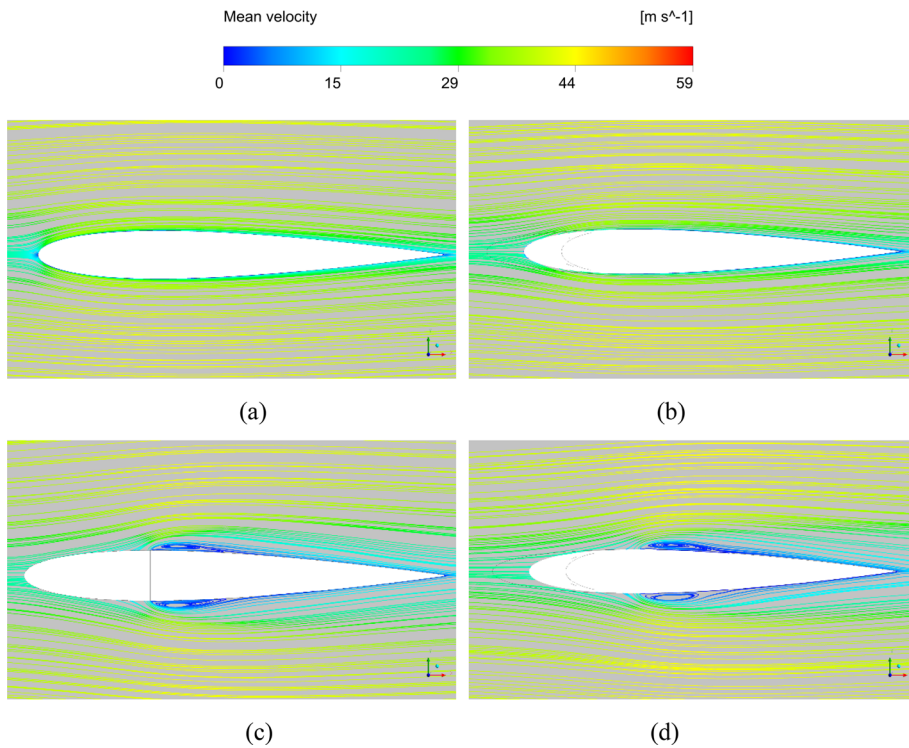


FIG. 16. Comparison of the time-averaged streamlines on the middle planes: (a) baseline, (b) A20W10, (c) porous, and (d) poro-A20W10.

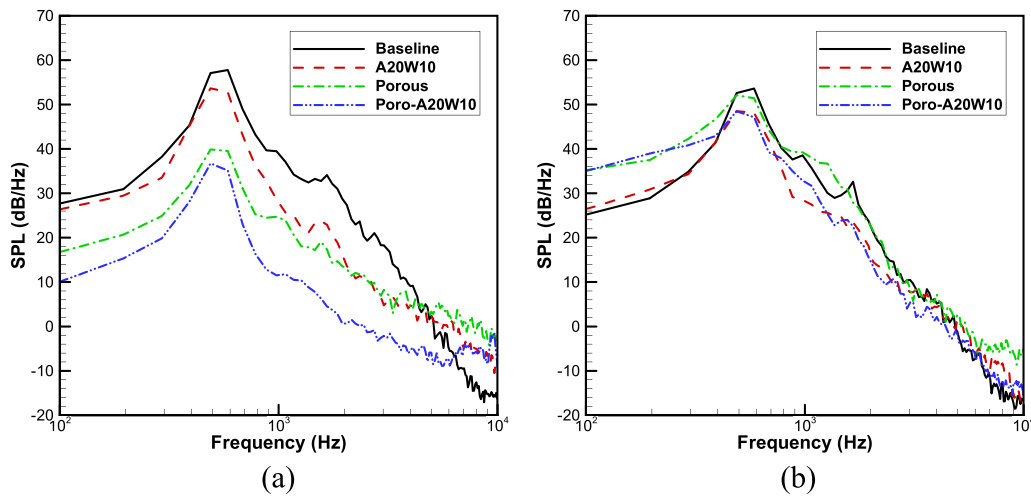


FIG. 17. Comparison of the SPL radiated by different parts of the baseline and bionic airfoils at  $\theta = 90^\circ$ : (a) the first 30% part of the airfoil, and (b) the last 70% part of the airfoil.

Fig. 18 for the baseline and bionic airfoils. The PSD is averaged over 49 spanwise monitor points for all the airfoils. It can be seen that, in almost the whole frequency range, the auto-power spectral density is reduced by the A20W10 and poro-A20W10 airfoil. The auto-power spectra density is decreased in the low-frequency range, while it is increased in the mid- to high-frequency range by the porous airfoil. The cross-power spectral density shown in Fig. 18(b) exhibits similar results with the auto-power spectral density. In general, the

poro-A20W10 obtains the largest fluctuating pressure reduction in the whole frequency range except for at very high frequencies.

The two-point temporal-spatial correlation coefficient of the pressure signal is defined by

$$R_{pp}(\Delta z, \Delta t) = \frac{\text{cov}(p(z, t), p(z + \Delta z, t + \Delta t))}{\sqrt{\text{var}(p(z, t))\text{var}(p(z + \Delta z, t + \Delta t))}}, \quad (21)$$

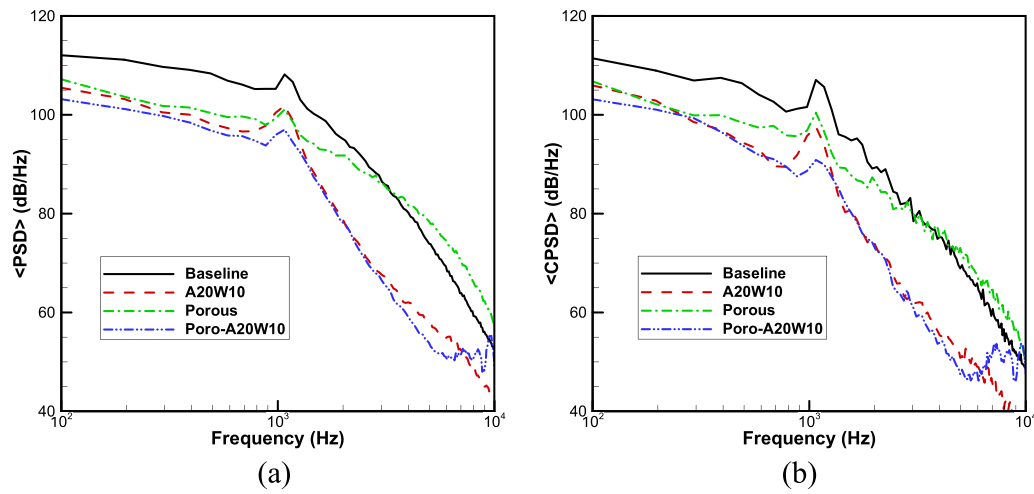


FIG. 18. Comparison of the spanwise averaged auto- and cross-power spectral density of fluctuating pressure: (a) auto-power spectral density and (b) cross-power spectral density.

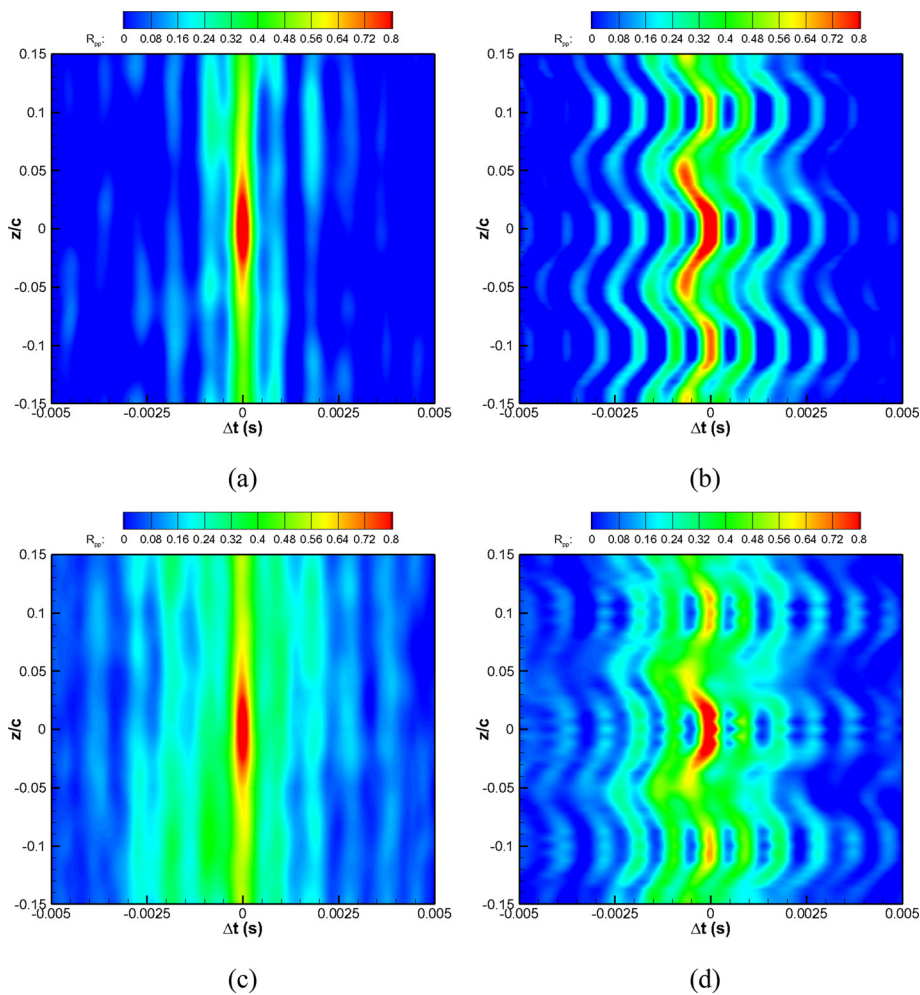


FIG. 19. Temporal-spatial correlation coefficient of pressure fluctuations at the leading edge of the airfoils: (a) baseline, (b) A20W10, (c) porous, and (d) poro-A20W10.

09 April 2024 10:28:22



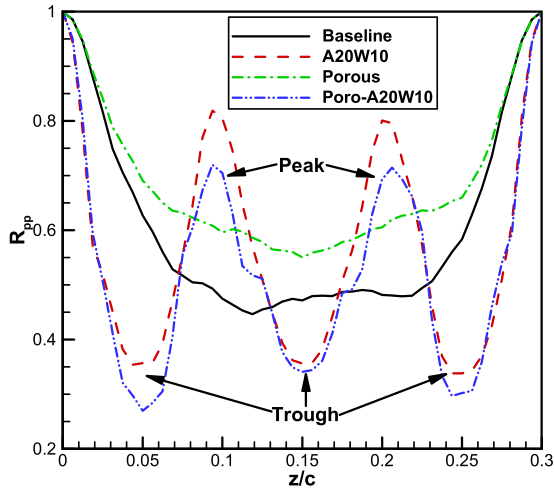


FIG. 20. Spanwise correlation coefficient of pressure fluctuations for the baseline and bionic airfoils.

where “cov” and “var” represent the covariance and variance of two pressure time signals, respectively. Figure 19 plots the temporal-spatial correlation coefficient of pressure fluctuations at the leading edge of the baseline and bionic airfoils. For the baseline and porous airfoils, straight distributions of the contours are observed along the span. The temporal-spatial correlations are slightly increased by the porous airfoil. For the A20W10 and poro-A20W10 airfoils, the correlation contours exhibit wavy patterns, which might induce destructive interferences.

The spanwise correlation coefficients can be directly obtained by setting  $\Delta t = 0$  in Eq. (21). The spanwise correlation coefficients at the airfoil leading edge are further depicted in Fig. 20 for the baseline and bionic airfoils. It is notable that the spanwise correlations are increased by the porous airfoil, which indicates that the spanwise de-correlation effect is not the main noise reduction mechanism for the porous airfoil.

For the A20W10 and poro-A20W10 airfoils, the spanwise correlations exhibit periodic characteristics, and the poro-A20W10 airfoil has a lower level than those of the A20W10 airfoil.

The spanwise coherence (magnitude squared) spectrum and phase spectrum are defined by

$$C_{pp}(z_1 : z_2, f) = \frac{|S_{pp}(z_1 : z_2, f)|^2}{|S_{pp}(z_1, f)| |S_{pp}(z_2, f)|}, \quad (22)$$

$$\phi_{pp}(z_1 : z_2, f) = \text{Im}[\log(S_{pp}(z_1 : z_2, f))], \quad (23)$$

where  $S_{pp}(z, f)$  and  $S_{pp}(z_1 : z_2, f)$  refer to the auto- and cross-power spectral density of the pressure fluctuations, respectively. “Im” and “log” denote the imaginary part of a complex number and the natural logarithm, respectively.

In order to analyze the overall spanwise coherence effects, the spanwise averaged coherence spectrum and phase spectrum are further defined by

$$\langle C_{pp}(f) \rangle = \frac{1}{N} \sum_{i=1}^N C_{pp}(z_1 : z_i, f), \quad (24)$$

$$\langle \cos[\phi_{pp}(f)] \rangle = \frac{1}{N} \sum_{i=1}^N \cos[\phi_{pp}(z_1 : z_i, f)], \quad (25)$$

where  $N$  is number of spanwise monitor points. In this study,  $\cos(\phi_{pp})$  is chosen as an indicator of phase interference instead of the raw phase difference. Therefore, the corresponding value is  $+1$  when the raw phase difference is an even multiple of  $\pi$  (in phase) and  $-1$  when it is an odd multiple of  $\pi$  (out of phase).

The spanwise averaged coherence spectrum and phase spectrum are plotted in Fig. 21 for the baseline and bionic airfoils. As shown in Fig. 21(a), the spanwise coherence is increased by the three bionic airfoils in the low-frequency range, while it is decreased by the A20W10 and poro-A20W10 airfoil in the middle frequency range. Comparable spanwise coherence is observed at mid- to high frequencies for all the four airfoils. However, the spanwise coherence is significantly increased by the poro-A20W10 airfoil in the high-frequency range,

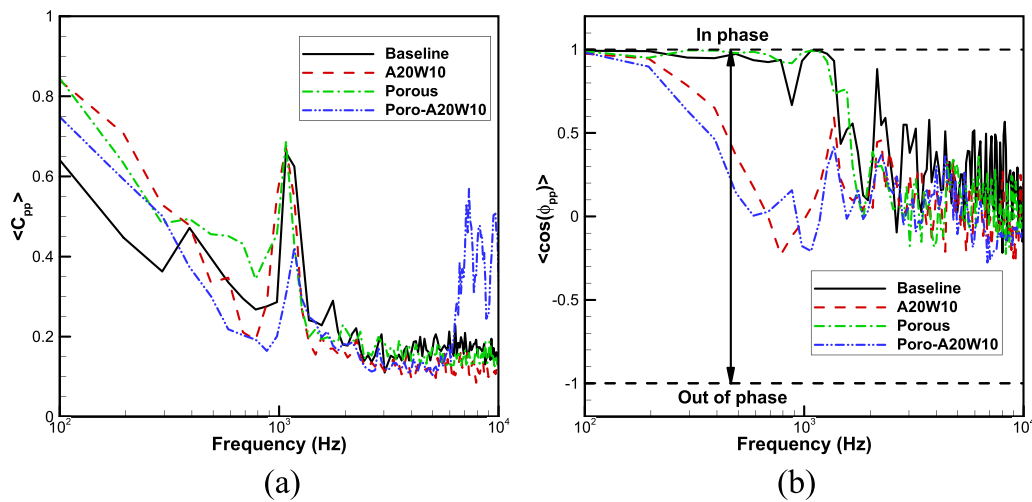


FIG. 21. Averaged profiles of the coherence spectra for the baseline and bionic airfoils: (a) averaged coherence spectrum and (b) averaged phase spectrum.

and the reason is still unclear. For the averaged phase spectrum shown in Fig. 21(b), it is found that the phase spectrum is considerably reduced by the A20W10 and poro-A20W10 airfoils in the low- to mid-frequency range, while the porous airfoil has comparable phase spectrum with the baseline airfoil in this frequency range. In the mid- to high-frequency range, all the four airfoils possess comparable values. It can be conjectured from Fig. 21 that the spanwise de-coherence effect is one of the main noise reduction mechanisms for the A20W10 and poro-A20W10 airfoils, while it contributes little to the noise reduction of the porous airfoil.

#### IV. CONCLUSIONS

A hybrid IDDES/FW-H acoustic analogy method is used to study the effect of three different bionic treatments on the airfoil turbulence interaction noise. The rod-airfoil flow configuration is chosen in this study with the rod wake interacting with a downstream airfoil to generate leading-edge noise. The flow fields around the rod and airfoil are computed using the improved delayed detached eddy simulation model, and the aerodynamic noise is predicted using the FW-H equation. The predicted aerodynamic and aeroacoustic results agree well with experimental data and previous studies.

The results show that the mean aerodynamic performance is degraded by all the three bionic treatments. The mean drag is increased by 28.5%, 335.9%, and 375.3%, respectively, by the A20W10, porous, and poro-A20W10 airfoils. In addition, the wake deficit and turbulence intensity are also enhanced by the three bionic treatments. However, the drag fluctuations are reduced by 13.3%, 72.1%, and 68%, and the lift fluctuations are reduced by 37.6%, 53.9%, and 61.4%, respectively, by the A20W10, porous, and poro-A20W10 airfoils.

Both the tonal noise and broadband noise can be mitigated by the three bionic treatments. The wavy A20W10 airfoil is more effective for broadband noise reduction, while the porous airfoil is more effective for tonal noise reduction. For the combined poro-A20W10 airfoil, it has both the advantages of the wavy airfoil and porous airfoil, and it can significantly reduce both the tonal noise and broadband noise. At the directivity angle of 90°, the tonal noise is reduced by 4.6, 10.2, and 12.2 dB by the A20W10, porous, and poro-A20W10 airfoils, respectively, while the broadband noise can be decreased by up to 10 dB by the poro-A20W10 airfoil. The OASPL can be reduced by 4.4, 8.8, and 11.5 dB by the A20W10, porous, and poro-A20W10 airfoils, respectively.

The noise reduction mechanisms are explored in detail for the three bionic treatments. The pressure fluctuations on the airfoil surface are considerably reduced by the A20W10 airfoil except for the trough region. For the porous airfoil, the pressure fluctuations on the airfoil leading edge achieve very low level. However, intensive pressure fluctuations are induced at the junction of the porous part and solid part. For the combined poro-A20W10 airfoil, the pressure fluctuations at both the leading-edge region and porous-solid junction region are significantly mitigated, resulting in the largest noise reduction level. The intensive pressure fluctuations around the junctions are induced by the separated flow at the junctions. The spanwise coherence is reduced by the A20W10 and poro-A20W10 airfoils, while it is increased by the porous airfoil. Therefore, the main noise reduction mechanisms of the porous airfoil is the source cutoff effect, while the main noise reduction mechanisms of the A20W10 and poro-A20W10 airfoils include both the source cutoff effect and the spanwise de-coherence effect.

The combined poro-wavy bionic treatment proposed in the present study has been proved to be a very promising passive noise control method. However, it should be noted that the aerodynamic performance is considerably degraded by the poro-wavy modification, which makes such a bionic treatment not that applicable. More studies should be conducted to find the optimal combination strategy.

#### ACKNOWLEDGMENTS

This work was supported by the National Natural Science Foundation of China (Nos. 52106056 and 52276038), the Fundamental Research Funds for the Central Universities (Nos. 501XTCX2023146001 and 3102021OQD706), the Science Center for Gas Turbine Project (Nos. P2022-A-II-003-001 and P2022-B-II-011-001), and the Laboratory of Aerodynamic Noise Control (No. ANCL20220101).

#### AUTHOR DECLARATIONS

##### Conflict of Interest

The authors have no conflicts to disclose.

##### Author Contributions

**Weijie Chen:** Conceptualization (equal); Writing – original draft (equal). **Hui Lei:** Validation (equal); Writing – review & editing (equal). **Yudi Xing:** Investigation (supporting); Software (equal). **Liangfeng Wang:** Conceptualization (supporting); Methodology (equal). **Teng Zhou:** Conceptualization (equal); Writing – review & editing (equal). **Weiyang Qiao:** Funding acquisition (lead); Supervision (equal).

#### DATA AVAILABILITY

The data that support the findings of this study are available from the corresponding author upon reasonable request.

#### REFERENCES

- <sup>1</sup>R. K. Amiet, "Acoustic radiation from an airfoil in a turbulent stream," *J. Sound Vib.* **41**(4), 407–420 (1975).
- <sup>2</sup>H. D. Meyer and E. Envía, "Aeroacoustic analysis of turbofan noise generation," NASA CR 1996-4715 (1996).
- <sup>3</sup>A. Epstein, "The lessons of P&W's geared turbofan (TM) engine and the implications for the future," in *International Symposium on Air Breathing Engines (ISABE)*, Phoenix, AZ, October 2015.
- <sup>4</sup>P. Chaitanya, P. Joseph, S. Narayanan, C. Vanderwel, J. Turner, J. W. Kim, and B. Ganapathisubramani, "Performance and mechanism of sinusoidal leading edge serrations for the reduction of turbulence-aerofoil interaction noise," *J. Fluid Mech.* **818**, 435–464 (2017).
- <sup>5</sup>P. Chaitanya, P. Joseph, S. Narayanan, and J. W. Kim, "Aerofoil broadband noise reductions through double-wavelength leading-edge serrations: A new control concept," *J. Fluid Mech.* **855**, 131–151 (2018).
- <sup>6</sup>S. Narayanan and S. K. Singh, "On the reductions of aerofoil-turbulence interaction noise through multi-wavelength leading edge serrations," *Proc. Inst. Mech. Eng., Part G* **235**(9), 1036–1052 (2020).
- <sup>7</sup>P. Chaitanya, P. Joseph, and L. J. Ayton, "Leading-edge profiles for the reduction of airfoil interaction noise," *AIAA J.* **58**(3), 1118–1129 (2020).
- <sup>8</sup>B. S. Lyu, J. L. Xu, T. F. Geyer, P. Chaitanya, Q. Q. Ye, J. H. Cui, and L. Ayton, "Experimental investigation into the acoustical superiority of ogee serrations in reducing leading edge noise," *Appl. Acoust.* **216**, 109722 (2024).

- <sup>9</sup>W. J. Chen, W. Y. Qiao, F. Tong, L. F. Wang, and X. N. Wang, "Experimental investigation of wavy leading edges on rod-aerofoil interaction noise," *J. Sound Vib.* **422**, 409–431 (2018).
- <sup>10</sup>S. H. S. Vemuri, X. Liu, B. Zang, and M. Azarpeyvand, "On the use of leading-edge serrations for noise control in a tandem airfoil configuration," *Phys. Fluids* **32**, 077102 (2020).
- <sup>11</sup>J. W. Kim, S. Haeri, and P. F. Joseph, "On the reduction of aerofoil-turbulence interaction noise associated with wavy leading edges," *J. Fluid Mech.* **792**, 526–552 (2016).
- <sup>12</sup>J. M. Turner and J. W. Kim, "On the universal trends in the noise reduction due to wavy leading edges in aerofoil-vortex interaction," *J. Fluid Mech.* **871**, 186–211 (2019).
- <sup>13</sup>W. J. Chen, W. Y. Qiao, F. Tong, L. F. Wang, and X. N. Wang, "Numerical investigation of wavy leading edges on rod-airfoil interaction noise," *AIAA J.* **56**(7), 2553–2567 (2018).
- <sup>14</sup>M. Buszyk, C. Polacsek, T. L. Garrec, R. Barrier, and C. Bailly, "Numerical assessment of turbulence-cascade noise reduction and aerodynamic penalties from serrations," *AIAA J.* **60**(6), 3603–3619 (2022).
- <sup>15</sup>F. Tong, W. Y. Qiao, K. B. Xu, L. F. Wang, W. J. Chen, and X. N. Wang, "On the study of wavy leading-edge vanes to achieve low fan interaction noise," *J. Sound Vib.* **419**, 200–226 (2018).
- <sup>16</sup>D. Casalino, F. Avallone, I. Martino, and D. Ragni, "Aeroacoustic study of a wavy stator leading edge in a realistic fan/OGV stage," *J. Sound Vib.* **442**, 138–154 (2019).
- <sup>17</sup>X. Huang, "Theoretical model of acoustic scattering from a flat plate with serrations," *J. Fluid Mech.* **819**, 228–257 (2017).
- <sup>18</sup>B. Lyu and M. Azarpeyvand, "On the noise prediction for serrated leading edges," *J. Fluid Mech.* **826**, 205–234 (2017).
- <sup>19</sup>L. J. Ayton and J. W. Kim, "An analytic solution for the noise generated by gust-aerofoil interaction for plates with serrated leading edges," *J. Fluid Mech.* **853**, 515–536 (2018).
- <sup>20</sup>L. J. Ayton and P. Chaitanya, "An analytical and experimental investigation of aerofoil-turbulence interaction noise for plates with spanwise-varying leading edges," *J. Fluid Mech.* **865**, 137–168 (2019).
- <sup>21</sup>B. Lyu, L. J. Ayton, and P. Chaitanya, "On the acoustic optimality of leading-edge serration profiles," *J. Sound Vib.* **462**, 114923 (2019).
- <sup>22</sup>B. Lyu and L. J. Ayton, "Rapid noise prediction models for serrated leading and trailing edges," *J. Sound Vib.* **469**, 115136 (2020).
- <sup>23</sup>R. Zamponi, S. Satcunanathan, S. Moreau, D. Ragni, M. Meinke, W. Schroder, and C. Schram, "On the role of turbulence distortion on leading-edge noise reduction by means of porosity," *J. Sound Vib.* **485**, 115561 (2020).
- <sup>24</sup>P. Chaitanya, P. Joseph, T. P. Chong, M. Priddin, and L. Ayton, "On the noise reduction mechanisms of porous aerofoil leading edges," *J. Sound Vib.* **485**, 115574 (2020).
- <sup>25</sup>S. P. Cabre, P. Chaitanya, P. Joseph, J. W. Kim, M. J. Priddin, L. J. Ayton, T. F. Geyer, and T. P. Chong, "Downstream porosity for the reduction of turbulence-aerofoil interaction noise," *J. Sound Vib.* **541**, 117324 (2022).
- <sup>26</sup>L. Bowen, A. Celik, B. Zhou, M. F. Westin, and M. Azarpeyvand, "The effect of leading edge porosity on airfoil turbulence interaction noise," *Acoust. Soc. America* **152**, 1437–1448 (2022).
- <sup>27</sup>R. Zamponi, S. Satcunanathan, S. Moreau, M. Meinke, W. Schroder, and C. Schram, "Effect of porosity on Curle's dipolar sources on an aerofoil in turbulent flow," *J. Sound Vib.* **542**, 117353 (2023).
- <sup>28</sup>A. Vathylakis and T. P. Chong, "Poro-serrated trailing-edge devices for airfoil self-noise reduction," *AIAA J.* **53**(11), 3379–3394 (2015).
- <sup>29</sup>T. P. Chong and E. Dubois, "Optimization of the poro-serrated trailing edges for airfoil broadband noise reduction," *J. Acoust. Soc. Am.* **140**(2), 1361–1373 (2016).
- <sup>30</sup>M. S. Gritskevich, A. V. Garbaruk, J. Schutze, and F. R. Menter, "Development of DDES and IDDES formulations for the  $k-\omega$  shear stress transport model," *Flow. Turbul. Combust.* **88**, 431–449 (2012).
- <sup>31</sup>K. Vafai, "Convective flow and heat transfer in variable-porosity media," *J. Fluid Mech.* **147**, 233–259 (1984).
- <sup>32</sup>C. T. Hsu and P. Cheng, "Thermal dispersion in porous medium," *Int. J. Heat Mass Transfer* **33**(8), 1587–1597 (1990).
- <sup>33</sup>B. Alazmi and K. Vafai, "Analysis of variants within the porous media transport models," *J. Heat Transfer* **122**, 303–326 (2000).
- <sup>34</sup>S. Ergun, "Fluid flow through packed columns," *Chem. Eng. Prog.* **48**(2), 89–94 (1952).
- <sup>35</sup>Y. Bae and Y. J. Moon, "Effect of passive porous surface on the trailing-edge noise," *Phys. Fluids* **23**, 126101 (2011).
- <sup>36</sup>J. E. Ffowcs Williams and D. L. Hawkings, "Sound generation by turbulence and surfaces in arbitrary motion," *Proc. R. Soc. London, Ser. A* **264**(1151), 321–342 (1969).
- <sup>37</sup>F. Farassat, "Derivation of formulations 1 and 1A of Farassat," NASA TM-2007-214853 (2007).
- <sup>38</sup>D. Casalino, M. Jacob, and M. Roger, "Prediction of rod-airfoil interaction noise using the Ffowcs-Williams-Hawkings analogy," *AIAA J.* **41**(2), 182–191 (2003).
- <sup>39</sup>J. Boudet, N. Grosjean, and M. C. Jacob, "Wake-airfoil interaction as broadband noise source: A large-eddy simulation study," *Int. J. Aeroacoust.* **4**(1), 93–116 (2005).
- <sup>40</sup>M. Caraeni, Y. Dai, and D. Caraeni, "Acoustic investigation of rod airfoil configuration with DES and FWH," AIAA Paper No. 2007-4106, 2007.
- <sup>41</sup>B. Greschner, F. Thiele, M. C. Jacob, and D. Casalino, "Prediction of sound generated by a rod-airfoil configuration using EASM DES and the generalised Lighthill/FW-H analogy," *Comput. Fluids* **37**(4), 402–413 (2008).
- <sup>42</sup>S. Galdéano, S. Barré, and N. Réau, "Noise radiated by a rod-airfoil configuration using DES and the Ffowcs-Williams & Hawkings' analogy," AIAA Paper No. 2010-3702, 2010.
- <sup>43</sup>A. Schell, "Validation of a direct noise calculation and a hybrid computation aeroacoustics approach in the acoustic far field of a rod-airfoil configuration," AIAA Paper No. 2013-2122, 2013.
- <sup>44</sup>J. C. Giret, A. Sengissen, S. Moreau, M. Sanjose, and J. C. Jouhaud, "Noise source analysis of a rod-airfoil configuration using unstructured large-eddy simulation," *AIAA J.* **53**(4), 1062–1077 (2015).
- <sup>45</sup>Y. Jiang, M. L. Mao, X. G. Deng, and H. Y. Liu, "Numerical investigation on body-wake flow interaction over rod-airfoil configuration," *J. Fluid Mech.* **779**, 1–35 (2015).
- <sup>46</sup>F. Tong, W. Y. Qiao, W. J. Chen, L. F. Wang, and X. N. Wang, "Broadband noise prediction using large eddy simulation and a frequency domain method," *Appl. Acoust.* **117**, 94–105 (2016).
- <sup>47</sup>B. R. Agrawal and A. Sharma, "Numerical analysis of aerodynamic noise mitigation via leading edge serrations for a rod-airfoil configuration," *Int. J. Aeroacoust.* **15**(8), 734–756 (2016).
- <sup>48</sup>B. Y. Zhou, T. Albring, N. R. Gauger, C. R. I. Da Silva, T. D. Economou, and J. J. Alonso, "Evaluation of different methods in computational aeroacoustics for noise prediction and minimization of a rod airfoil configuration," in The 24th International Congress on Sound and Vibration, London, United Kingdom, 2017.
- <sup>49</sup>L. S. Rousoulis, C. Lacor, and G. Ghorbaniasl, "A flow control technique for noise reduction of a rod-airfoil configuration," *J. Fluids Struct.* **69**, 293–307 (2017).
- <sup>50</sup>S. Sharma, T. Geyer, E. Sarradj, and H. Schmidt, "Numerical investigation of noise generation by rod-airfoil configuration using DES (SU) and the FW-H analogy," AIAA Paper No. 2019-2400, 2019.
- <sup>51</sup>S. R. L. Samion and M. S. M. Ali, "Comparison of rod-airfoil noise calculation between large eddy simulation (LES) and detached-eddy simulation (LES)," *CFD Lett.* **11**(2), 12–20 (2019).
- <sup>52</sup>Y. Li, Z. W. Chen, and X. N. Wang, "Flow/noise control of a rod-airfoil configuration using "natural rod-base blowing": Numerical experiments," *Eur. J. Mech. B* **83**, 99–113 (2020).
- <sup>53</sup>Y. Jin, F. Liao, J. S. Cai, and P. J. Morris, "Investigation on rod-airfoil noise with high-order cell-centered finite difference method and acoustic analogy," *Aerosp. Sci. Technol.* **102**, 105851 (2020).
- <sup>54</sup>S. Sharma, T. F. Geyer, and J. Giesler, "Effect of geometric parameters on the noise generated by rod-airfoil configuration," *Appl. Acoust.* **177**, 107908 (2021).
- <sup>55</sup>C. H. Yang, H. Y. Feng, Y. H. Peng, F. Tong, and N. Bao, "Numerical investigation of rod-airfoil interaction noise reduction using cylindrical collar," *Acoust. Soc. Am.* **151**, 3641–3653 (2022).
- <sup>56</sup>J. T. Han, Y. Zhang, S. Y. Li, W. R. Hong, and D. Z. Wu, "The noise-generating mechanism of rod-airfoil configuration and the effect of spanwise length on noise prediction," *Aerosp. Sci. Technol.* **134**, 108166 (2023).

- <sup>57</sup>B. Y. Zhou, T. Albring, N. R. Gauger, C. R. I. da Silva, T. D. Economon, and J. J. Alonso, "Reduction of airframe noise components using a discrete adjoint approach," AIAA Paper No. 2017-3658, 2017.
- <sup>58</sup>W. Q. Zhu, Z. X. Xiao, and S. Fu, "Numerical modeling screen for flow and noise control around tandem cylinders," *AIAA J.* **58**(6), 2504–2516 (2020).
- <sup>59</sup>P. D. Welch, "The use of fast Fourier transform for the estimation of power spectra: A method based on time averaging over short, modified periodograms," *IEEE Trans. Audio Electroacoust.* **15**, 70–73 (1967).
- <sup>60</sup>J. Boudet, "Approches numériques pour la simulation du bruit à large bande en vue de L'application aux turbomachines." Ph.D. thesis (École Centrale de Lyon, Écully, France, 2003).
- <sup>61</sup>W. J. Chen, K. S. Xiang, L. F. Wang, F. Tong, and W. Y. Qiao, "Extended aeroacoustic spanwise correction method for the aerodynamic noise prediction of large-span objects," *Proc. Inst. Mech. Eng., Part G* **237**(3), 660–671 (2022).
- <sup>62</sup>N. Curle, "The influence of solid boundaries upon aerodynamic sound," *Proc. R. Soc. London, Ser. A* **231**(1187), 505–514 (1955).
- <sup>63</sup>A. Lau, S. Haeri, and J. W. Kim, "The effect of wavy leading edges on aerofoil-gust interaction noise," *J. Sound Vib.* **332**, 6234–6253 (2013).
- <sup>64</sup>C. Teruna, F. Avallone, D. Casalino, and D. Ragni, "Numerical investigation of leading edge noise reduction on a rod-airfoil configuration using porous materials and serrations," *J. Sound Vib.* **494**, 115880 (2021).